NMAMIT

NITTE

Annual Research Journal

Volume 3 October 2013 ISSN 2249-0426

Published by:
NMAM Institute of Technology
Nitte - 574 110
www.nitte.ac.in/nmamit

EDITORIAL

I am happy to note that NMAMIT is bringing out 3rd volume of Annual Research Journal. Thanks to all the contributors.

The Current century has been witnessing scientific explosion and development of technology in many fields. To mention a few- soil stabilization, Green buildings, Image processing, Embedded systems etc.,

I am happy to note that a large number of teachers in higher educational Institutions in India are involved in research. Even though presently in India research are carried out not on the cutting edge topics, it will be good if they could at least contribute towards the development of rural areas. In this direction more and more number of researches must be carried out to help and support our poor farmers as India is made up of villages. As a whole whether research is carried out on cutting edge topic or not, the result must be beneficial to the rural masses.

Dr. Niranjan N. Chiplunkar
Editor-in-Chief

MEMBERS OF EDITORIAL BOARD

EDITOR-IN-CHEIF

Dr. Nirajnjan N. Chiplunkar
NMAM Institute of Technology, Nitte

EDITOR

Dr. Sudesh Bekal
Dean (R&D), NMAM Institute of Technology, Nitte

EDITORIAL BOARD

Dr. S. Y. Kulkarni
M. S. Ramayya Institute of Technology, Bangalore

Dr. N. S. Sriram
Vidya Vikas College of Engineering., Mysore

Dr. C. Vaman Rao
NMAM Institute of Technology, Nitte

Dr. Seetharam Shettigar
NMAM Institute of Technology, Nitte

Dr. Ashok Babu T. P.
National Institute of Technology Karnataka, Suratkal

Dr. Ujwal P.
NMAM Institute of Technology, Nitte

Dr. Jaganath Nayak,
National Institute of Technology Karnataka, Suratkal

Dr. Shridhara S.,
Indian Institute of Technology Bombay, Mumbai

Dr. K. V. V. Murthy,
Indian Institute of Technology, Gandhinagar

Dr. Navakanth Bhat,
Indian Institute of Science & Communication, Bangalore

Dr. Gopalakrishna Kini,
Manipal Institute of Technology, Manipal

Dr. Khalid, Vellur Institute of Technology, Vellur

EDITORIAL ASSISTANT

Prof. Vinayaka B. Shet, NMAMIT, Nitte.

OUR REVIEWERS FOR THE YEAR 2013

Dr. Gangadharan, NITK, Surathkal
Dr. Sreedhara S., IITB, Mumbai
Dr. Behrooz Nowrouzian, Alberta University, Canada
Dr. Hegui Zhu, Jilin University, Changchun,China
Dr. Qinkai Han, Tsinghua University, Beijing,China
Dr. Amith Kumar, Alberta University, Canada

NMAMIT

Annual Research Journal

Volume 3

October 2013

ISSN 2249-0426

Published by:

NMAM Institute of Technology

An Autonomous Institution Under VTU, Belgaum

(A Unit of Nitte Education Trust)

NITTE - 574 110, UDUPI DIST., KARNATAKA

wb : www.nitte.ac.in/nmamit

© NMAM Institute of Technology, Nitte

NMAMIT Annual Research Journal Volume No. 3

October 2013

ISSN : 2249-0426

Published by :

NMAM Institute of Technology

Nitte, 574 110

Udupi district, Karnataka State, India

www.nitte.ac.in/nmamit

Printed by :

Praveena Mudrana

Karkala 574104,

Udupi district, Karnataka State

email: praveenamudrana@gmail.com

A New Visual Cryptographic Scheme Using Mixed Key Generation and Residue Number System based on Chinese Remainder Theorem

Ranjan Kumar H S[#1], Prasanna Kumar H R[#2], Sudeepa K B[*3], Ganesh Aithal[*4]

[#]*CSE Department, NMAMIT, Udupi, India*
[1]raanj85@gmail.com
[*]*CSE Department, PACE, Mangalore, India*
[3]hegde_pace@yahoo.co.in

***Abstract*-With the rapid development of internet, transfer of data reliably and securely has become one of the challenges. In this paper we have introduced a novel visual cryptographic technique. This method is applicable for both Color and Grayscale images. This method uses the concept of Residual Number System (RNS) based on Chinese Remainder Theorem (CRT) for share creation and share stacking of a given image. A pixel (8 bit) of an image is taken and added with an eight bit key to get a cipher pixel. The algorithm used is additive mod 255.The key is generated using a pseudo random number generator and Mixed Key Generation technique. After encryption the cipher pixel is mapped into a Residue Number System of *'n'* Shares. These *'n'* Shares are stored or transmitted to the destination. The proposed approach like any other visual cryptographic approach is very secure, efficient, reliable, fast and easy to implement. Lastly, performance analysis of this visual cryptographic technique is done with respect to many metrics.**

***Keywords*-- Visual Cryptography, Sharing, Stacking, Residue Number System, Chinese Remainder Theorem, Mixed Key Generation**

I. INTRODUCTION

Visual Cryptography is one of the cryptographic methods of sharing data but it is applied only for image format. Many works in this area have been done and several algorithms have been developed. In 1994 Naor and Shamir [1] Proposed Visual Cryptography Scheme (VCS) which is a simple and secure method that allows sharing of secret without the need of any cryptographic computations. To encode the image, original image is split into *n* modified versions referred as shares. Decoding can be done by simply stacking subset *s* of those *n* shares. Figure 1 depicts the working of Visual Cryptography. The easiest way to implement visual cryptography is to print the two shares onto a transparent sheet.vcs is achieved by following access structure: [2]

1 :(2, 2) Visual Cryptographic Scheme (VCS)—this is a very simplest VCS scheme in which secret image is encrypted into 2 shares. To reveal the secret image 2 shares are overlaid or combined.

2 :(2, *n*) Visual Cryptographic Scheme (VCS)—this scheme encrypts the secret image into *n* shares such that when any two (or more) shares are overlaid the secret image is revealed.

3 *:(n, n*) Visual Cryptographic Scheme (VCS)—this scheme encrypts the secret image into *n* shares such that it can be revealed only when all *n* shares are overlaid.

4 :(*k, n*) Visual Cryptographic Scheme (VCS)—this scheme encrypts the secret image into *n* shares such that when at least *k* shares are combined secret image can be revealed.

A. VCS Algorithms

VCS Scheme normally involves two algorithms [3]:

- Algorithm for creating shares
- Algorithm for combining shares

VCS algorithm's efficiency is very critical factor and reliability and level of security are some more metric which we need to consider while designing a VCS algorithm. The VCS system should be reliable enough such a way that intruders are not able to read

the original image. One important functional requirement of any VCS system is size of shares which should be same as that of original image to prevent doubt for unauthorized user. Throughput of visual cryptographic algorithms is very important criteria such that share creation and stacking time should be significantly less. The VCS should be very simple but very difficult to break. Many algorithms developed in this area which is hot research subject.

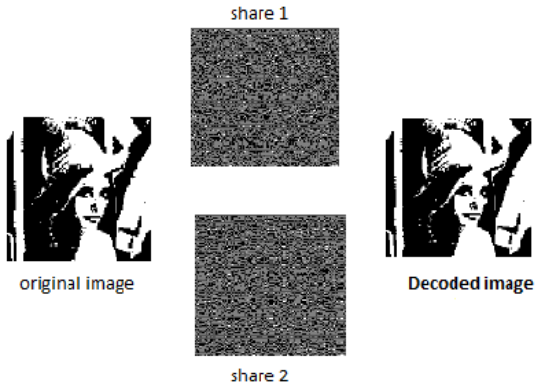

Fig. 1: Basic VCS Scheme

Algorithm for creating shares

This algorithm divides secret image into n number of shares. The shares created by this algorithm will be in unreadable format such that it is impossible to reveal secret image. Single share cannot reveal the secret image. If these individual shares are transmitted separately through communication network, security is achieved.

Algorithm for combining shares

This algorithm reveals the secret image by taking the number of shares as input. Some algorithm may take all shares as input and some other algorithm may take subset of shares as input. Decryption is done by merging shares which has taken as input.

II. Proposed System

Visual Cryptography is a technique to make data secure. After dividing image into *'n'* shares, the individual shares are sent via different communication channels to destination such that intruder has less chance to get whole information. However the VCS's are not Perfect Secure System, because intruder may gain access to all communication channels and might retrieve all shares.

This paper proposes a solution for above security issue by encrypting the Secret image using symmetric encryption method before share creation. If intruder now gets all share, since Secret image itself is encrypted he or she might not get any of the information.

Our novel VCS technique is a 3 out of 3 approach in which a secret image after encryption by symmetric method is divided into 3 shares and in order to decrypt the secret image we must have 3 shares. Figure 2 gives the architecture of our approach.

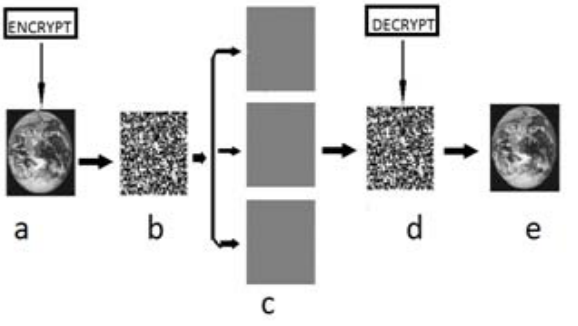

Fig. 2: Proposed Arc hitecture

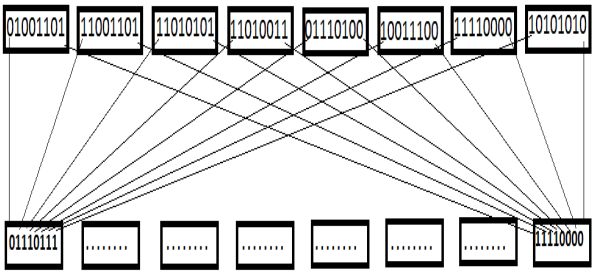

Fig. 3: Key Generation

First, for encryption additive modulo 255 algorithms is used. Keys are generated using a unique technique called Mixed Key Generation (MKG). In this method block of size of 8 byte keys are generated using PRN generation algorithm and individual bits from every byte is selected, since we have 8 byte word we can perform parallel operation with 8 byte of source data. Structure of Key generation technique is given in figure 3.By taking the keys generated by MKG method each pixel is encrypted to form Cipher pixel. Since, we can generate 8 keys at a time this improves the efficiency of cipher pixel generation. The algorithm is given in table 1.

Next, for share creation we are using Residual Number System (RNS) and for share stacking RNS based Chinese Remainder System (CRT) is used. The algorithms for the same are shown in table 2 and table 3 respective

TABLE 1:
ENCRYPTION ALGORITHM

Step 1: Generate 64 bit number using PRNG algorithm. Step 2: Apply MKG algorithm to select 8 keys of 1 byte each. Step 3: Encrypt 8 individual bytes of secret image using 8 keys generated in step 2. Step 4: Repeat step 1-3 until all pixels of secret image are encrypted

TABLE 2
SHARE GENERATION ALGORITHM

Step 1 : select 3 prime numbers m1,m2,m3 such that their product is greater than 255 and gcd of selected 3 numbers is 1(i.e. relatively prime) Step 2 : calculate r_{i1}=X mod m1 r_{i2}=X mod m2 r_{i3}=X mod m3 Where, r_{i1}, r_{i2}, r_{i3} are residues of *i'th* pixel of share 1, 2 and 3 respectively; X is an individual pixel; m_1, m_2 and m_3 are selected prime numbers. Step 3: Represent the residues r_{i1}, r_{i2}, r_{i3} as *i'th* pixel of share 1 2 and 3 respectively. Step 4: Repeat step 2 and 3 until all pixels are processed.

Example for share generation using algorithm in table 1

For example consider a pixel value x=128 and selected modulus m_1, m_2 and m_3 is 3, 5, and 17 respectively. Applying above rule we get r_{i1}=1, r_{i2}=3 and r_{i3}=9.So if the first pixel value of original image is 128 this value is mapped to 1 of first share,4 of second share and 1 of third share respectively.

Example for share stacking using algorithm in table 2

Dynamic range M=3×5×17=255

A_1 = 255/3 = 85

A_2 = 255/5 = 51

A_3 = 255/17 = 15

Next we have to calculate inverse

i.e

85 × 1 mod 3 = 1, so T_1=1

51×1 mod 5 = 1, so T_2=1

15×7 mod 17 = 1, so T_3=8

Using all these data we can get back original pixel *'x'*

$$x = (85\times1\times2 + 51\times1\times3 + 15\times8\times9) \bmod 255$$

$$= 1403 \bmod 255$$

$$x = 128$$

TABLE 3
SHARE STACKING ALGORITHM

Step 1: Calculate the dynamic range M=$m_1.m_2.m_3$ Step 2: Calculate $A_i = M/m_i$ Step 3: Find the solution of congruence's $A_i.T_i \bmod m_i$ Where T_i is multiplicative inverse of A_i Step 4: We can get back original pixel by CRT using below equation $x = \sum_{i=1}^{N} A_i.T_i.r_i \bmod M$ Step 5:Repeat step 4 until all pixels of shares are processed.

III TEST RESULTS

This visual cryptographic technique has been implemented using jdk.6.0_17.

A Encryption Process:

Fig. 4: (a) Original Image (b) Encrypted Image

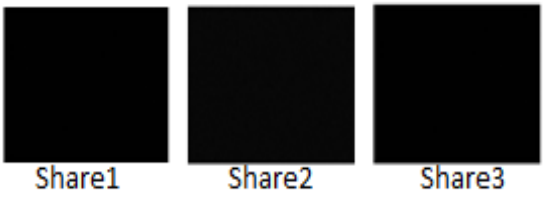

Fig. 5: Output of Share Creation Algorithm

Fig. 6: (a) Output of Stacking Algorithm (b) Reconstructed Image

We gave Figure 4.a as input for Symmetric Encryption Algorithm and we got Figure 4.b as output. By comparing original image and the encrypted image there is no visual information observed in the encrypted image. Next we gave encrypted image as input to stack generation algorithm and we got Figure 5 as output.

B Decryption Process:

At destination share stacking algorithm given in table 3 is run. Input to this algorithm is shares which are generated as in figure 5 and we got Figure 6.a as output. This algorithm is exact reconstruction algorithm which does not have any data loss. This algorithm is very efficient which has less execution time.

Next we gave Figure 6.a as input to Symmetric decryption algorithm and we got Figure 6.b as output.

By Comparing Figure 4.a and Figure 6.b we concluded that reconstructed image is exact copy of original image and there is no loss of information.

IV. PERFORMANCE ANALYSIS OF MKG

Before creating shares by VC technique since secret image itself is encrypted using Symmetric key approach, Performance analysis of the same in terms of Histograms, Visual testing, Key sensitivity analysis, Avalanche effect, Entropy and Standard deviation is done in this section and the results are as below[4].

A Histogram analysis

The Histogram of original image and corresponding encrypted image is shown in figure 7 and figure 8. It is clear that the histogram of the encrypted image is nearly uniformly distributed, and significantly different from the histogram of the original image. So, the encrypted image does not provide any clue to employ any statistical attack on the proposed encryption of an image procedure, which makes statistical attacks difficult. These properties tell that the proposed image encryption has high security against statistical attacks.

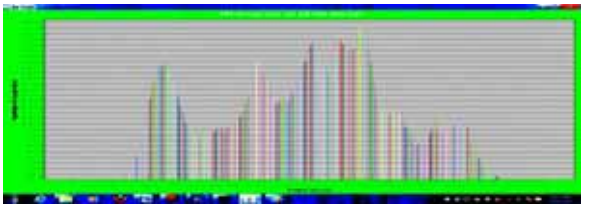

Fig. 7: Histogram of Original image

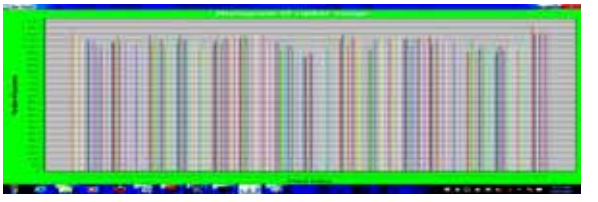

Fig. 8: Histogram of Cipher image using MKG

B. Visual testing

Lena and Cameraman images are encrypted and decrypted by the proposed method, and visual test is performed. Two examples are shown in Figure 9.a and Figure 9.d, with 512 x 512 sizes. By comparing the original and the encrypted images in Figure 9, there is no visual information observed in the encrypted image.

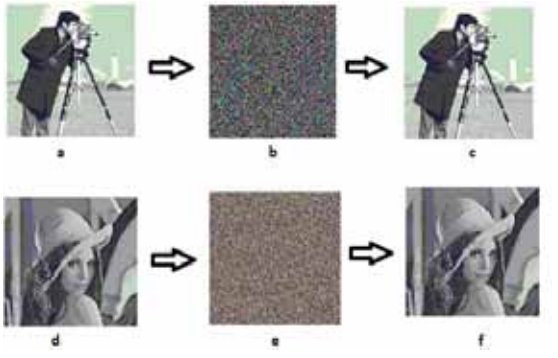

Fig. 9 : Visual testing outputs: (a) and (d) the original image of Cameraman and Lena stego-image, (b) and (e) respectively shows the encrypted image, (c) and (f) respectively show the decrypted image.

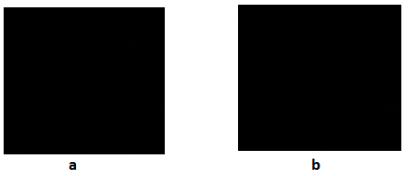

Fig. 10: Difference output: (a) show the difference between original image figure 9(a) and decrypted image figure 9(c). (b) Show the difference between original image figure 9(d) and decrypted image figure 9(f).

Difference between original images and their decrypted images shown in Figure 10, proves that, there is no loss of information, since the difference is always 0.We can also confirm this fact by checking the histograms of 10.a and 10.b respectively as in Figure 11 and 12.

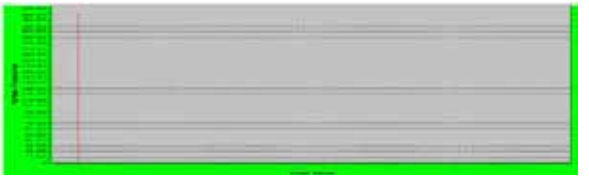

Figure 11 Histogram of Figure 10.a

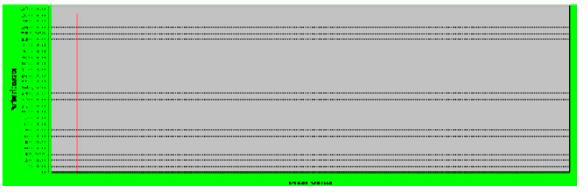

Fig. 12 Histogram of fig 10.b

C. Key Sensitivity Analysis

High key sensitivity is required by secure image cryptosystems, which means the encrypted image cannot be decrypted correctly even if there is only a small difference between the encryption and decryption keys. In the key sensitivity tests, we change one bit of the key. Figure 13 show key sensitivity test result. It can be observed that the decryption with a slightly different key (different secret key or initial values) fails completely. Therefore, the proposed image encryption scheme is highly key sensitive.

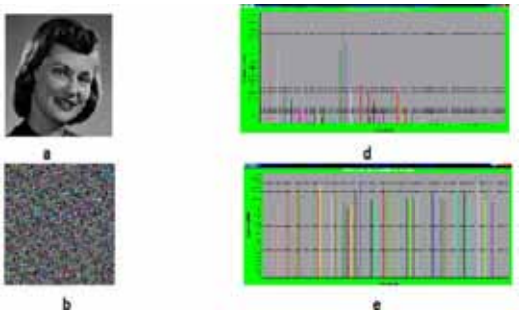

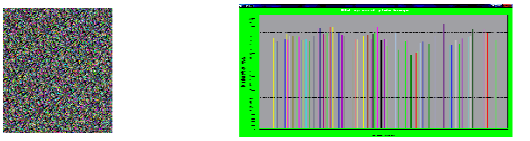

Fig. 13:Sensitivity analysis: (a) original image of girl face image (d) histogram of original image (b) encrypted image, (e) histogram of encrypted image (c) decrypted image with a bit changed,(f) histogram of decrypted image with a bit changed.

D. Noise Analysis

We also tested the resistance of our mixed key cryptosystem to the noise by adding to the cipher-images a noise. For the cipher-image in the Figures 9.b, we added a noise of the same size of plain-images. Noise image is generated using random number generator function of mean 0 and standard deviation 1.A cipher image after adding noise is given as input to decryption algorithm, by observing output of decryption algorithm as in Figure 14 we concluded that after adding noise to cipher image decryption is possible and is ideal.

Fig. 14 Noise Analysis: (a) show cipher image 6b with noise added, (b) show decrypted image.

E. Entropy and Standard Deviation

TABLE 4

QUANTITATIVE ANALYSIS

S .no	Image Name	Entropy	Standard Deviation
1	Lena	7.994	1.853
2	Girl face	7.896	2.123

Higher value of entropy indicates security against statistical attack. It is shown in table 4 that the entropy of proposed system is 7.994 and 7.896 and hence it is immune to statistical attack.

Small value of standard deviation of number of occurrences of cipher pixels implies that all cipher pixels occurs almost equal number of times. It is found that standard deviation of number of occurrences of

cipher text of the proposed scheme is small and we can conclude that the proposed cryptosystem is ideal.

F. Avalanche Effect

A small change in key or plaintext image should cause significant change in the corresponding cipher text image. This property of cryptosystem is known as avalanche effect. Avalanche effect is desirable property for all cryptographic algorithms. Strict avalanche effect occurs when a single bit change in the plaintext image change 50% of the bits in the cipher text image [4].As we can see in Figure 15 a single bit change in the initialization vector of feedback shift register will produce entirely different cipher pixels.

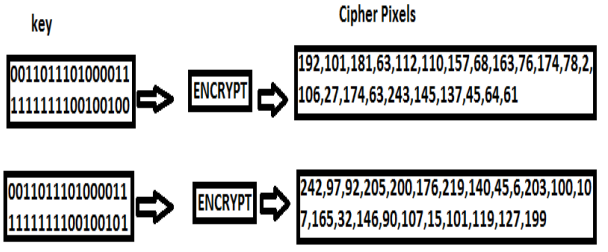

Fig. 15: Avalanche effect

V. SECURITY OF PROPOSED SCHEME

The proposed scheme is ideal since two popular techniques (Symmetric Encryption & Visual Cryptography) are combined. Major drawback of visual cryptography is that secret image can be revealed if intruder can access all communication channels such that he/she may get all shares which are transmitted through network. This method masks this problem since the secret image is encrypted by MKG technique before share creation. If intruder can access all channels now he/she may get only encrypted image and since we proved the security of encrypted image in previous section, we can conclude as a whole the proposed scheme is very secure.

VI FUTURE SCOPE

This paper contains some details about Visual Cryptography Scheme. If lossless Image compression methodology is applied before encryption we can strengthen cryptographic security. Because compressed image has less redundancy than the original image, cryptanalysis will be difficult [5].

VII. CONCLUSION

This paper proposes a new Key Generation called MKG and gives some details about how RNS based CRT and MKG can be employed for visual cryptography thereby improving security of existing VCS. The performance analysis proved that MKG is ideal against all kinds of attacks.

REFERENCES

[1] A. Shamir and M. Naor," Visual Cryptography," Advances in Cryptography -EUROCRYPT'94, Lecture Notes in Computer Science 950, 1995, pp. 1-12.

[2] G. Ateniese, C. Blundo, A. De Santis, and D. R.Stinson, Visual Cryptography for General Access Structures, Information and Computation, Vol. 129,No. 2, (1996), pp. 86-106

[3] S.Manimurugan,K.Porkumaran "A New Fast And Efficient Visual Cryptographic Scheme With Forgery Detection" Proceedings of ICETECT 2011

[4] Jawad Ahmad and Fawad Ahmed, "Efficiency Analysis and Security Evaluation of image Encryption Schemes "International Journal of Video & Image Processing and Network Security IJVIPNS-IJENS Vol: 12 No: 04, pp: 18-24.

[5] William Stallings "Network Security and Essentials" Third edition 2009

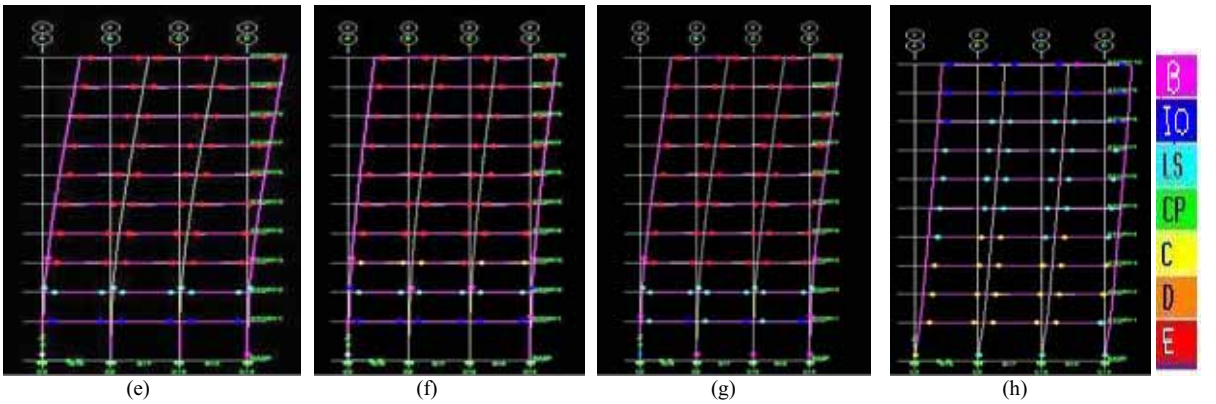

(e) (f) (g) (h)

Fig. 5.Deformed Shape of RC Frame for Pushover Load- EQX: (e) Without Diaphragm (f) With Semi rigid Diaphragm (g) With Rigid Diaphragm (h) With Shell element.

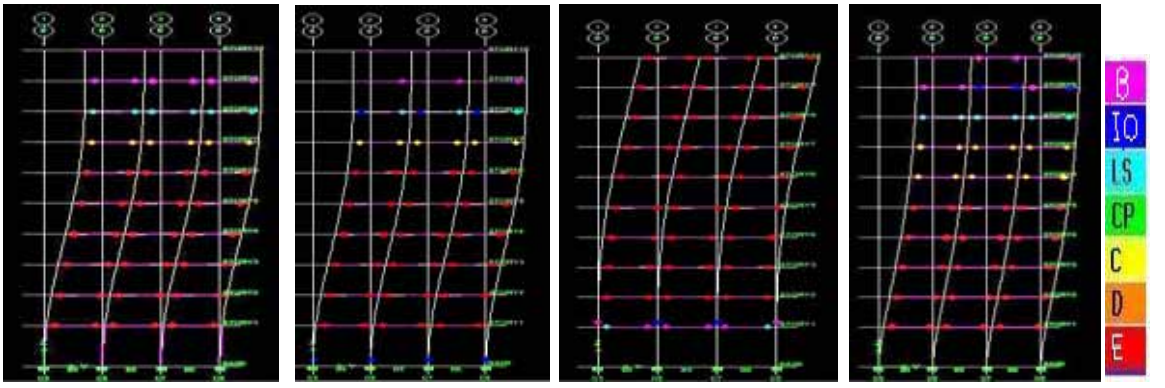

(i) (j) (k) (l)

Fig. 6.Deformed Shape of RC Frame for Pushover Load- Mode-1: (i) Without Diaphragm (j) With Semi rigid Diaphragm (k) With Rigid Diaphragm (l) With Shell element.

Comparative Study of Nonlinear Static Pushover Analysis of Space Frame with Different Diaphragms

Dr. Kiran Kamath[#1], Pranamya K[*2], Karthik Nayak[*3]

[#] *Professor, Department of Civil Engineering, Manipal Institute of Technology, Manipal, India.*

[1]kiran.kamath@manipal.edu

[*]*PG Students in Structural Engineering, Department of Civil Engineering*

Manipal Institute of Technology, Manipal, India.

[2]pranamya_k@yahoo.co.in

***Abstract*— This paper presents a comparative study of static nonlinear push over analysis on an existing RC frame structure with different diaphragm stiffness for the models in which the slabs were modeled as shell, membrane with rigid diaphragms, membrane with semi-rigid diaphragms and without any diaphragms. Non-linear pushover analyses were performed considering moderate seismic zone (zone-iii) of India. It is observed that the seismic demand at the soft storey level is significantly large when slab is modeled as shell element, with larger base shear and larger displacements compared with the models considered.**

***Keywords*—NonlinearStaticPushoverAnalysis, Diaphragms, PerformancePoint, Ductility .**

I. INTRODUCTION

The existing building can become seismically deficient since seismic design code requirements are constantly upgraded and advancement in engineering knowledge. They do not give the performance of non-structural components either provide difference in performance between the different structural system. This lead to the evolution of multilevel performance based design approaches. Among different approaches described, nonlinear static (pushover) analysis is very popular because of its simplicity and ability to estimate component and system level deformation demands with acceptable accuracy without intensive computational and modeling effort as dynamic analysis.

The slabs are normally considered as the medium to transfer the vertical area loads but rigidity of slabs contribute majorly on the overall seismic performance of the structure. Normally a slab behaves as horizontal diaphragm acting monolithically with beam and contributes additional stiffness and strength while resisting lateral loads. But rigidity of this diaphragm may vary due to provisions for ducts or huge opening in slabs for architectural and functional purposes. Hence its contribution to the overall seismic performance of the frame majorly depends on the flexibility of these diaphragms in distribution of lateral loads to horizontal force resisting elements.

In the present study we have done a comparative study on a simple RC framed structure with slab modeled as shell, rigid, semirigid diaphragms and without any diaphragm.

II. LITERATURE REVIEW

Uva et al., (2012) have considered the participation of masonry infill panel to overall seismic resistance of building. They have modeled the infill panel as equivalent strut of width bw using different mathematical models and compared the result. Mehmet Inel et al.(2006) carried out push over analysis using SAP-2000 comparing the performance of the building for default hinge properties and user defined hinge properties. They have concluded that the result obtained from user defined hinge properties are more accurate than of default hinges. Poluraju et al., (2011) using nonlinear pushover analysis evaluated the performance of G+3 building using SAP-2000.The results obtained from the study show that properly detailed and designed frame will perform well under seismic loads. Deshpande et al.,(2010) investigated the behavior of various alternative models of reinforced concrete moment resisting frame building with an open first storey and unreinforced masonry infill in the upper stories. They have suggested promote safety without too much changing the constructional practice of reinforced concrete structures. Kamath et al., (2012), investigated the behavior of various models of reinforced concrete moment resisting frames with soft storey at different floor levels. They found that as the location of soft storey moves from ground floor to top floor, the displacement at the top most floor level reduces significantly. The available literature indicates that the pushover analysis has not been considered with the slab stiffnesses.

III. DESCRIPTION OF RC FRAME BUILDING

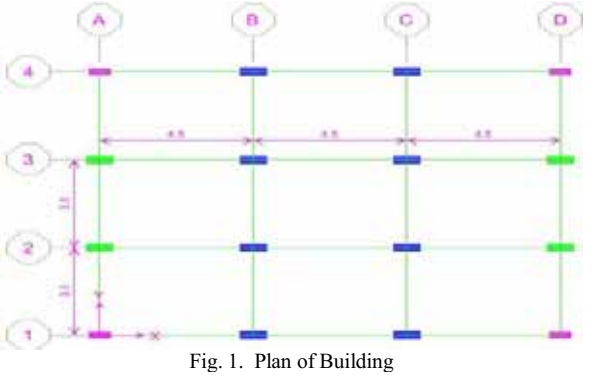

Fig. 1. Plan of Building

Three dimensional reinforced concrete moment resisting frame building with open ground floor and infilled with brick masonry in the top stories. The plan of the building is shown in Figure-1.The building consists of G+9 stories. All columns in all models are assumed to be fixed at the base for simplicity. The height of ground floor is 4.0m and upper storey heights are 3.0m. Slabs were modeled as shell, membrane with semirigid and rigid diaphragm element of 0.13m thickness for all stories for the different models considered. Live load on floor is taken as 3kN/m^2 and on roof is 1.5kN/m^2.Floor finish on the floor is 1kN/m^2.Weathering course on roof is 2kN/m^2.The seismic weight is calculated conforming to IS 1893-2002. The unit weights of concrete and masonry are taken as 25kN/m^3 and 20kN/m^3 respectively. The grade of concrete for column is M-25 and for beam and slab M-20.The building is special moment resisting frame considered to be situated in seismic zone III and intended for residential use. Building has no walls in ground floor and external wall thickness is taken as 230mm and internal wall thickness is taken as 110mm.The medium type of soil is considered and time period of the building in X-direction and Y-direction are 0.7593sec and 0.861sec respectively. Load combination considered for the linear static analysis for the design:

i. DL+LL
ii.1.5*(DL+LL)
iii1.2*(DL+LL±EQX)
iv.1.2*(DL+LL±EQY)
v. 1.5*(DL±EQX)
vi. 1.5*(DL±EQY)
vii. 0.9DL±1.5EQX
viii 0.9DL±1.5EQX

DL-Dead Load, LL-Live Load, EQX-Earth Quake in X-direction, EQY- Earth Quake in Y-direction.

As per the combination the designed section sizes are as follows.

Beam size is 230mmX450mm.Size of Column: C1-230mmX600mm,C2-300mmX750mm,C3-300mmX750mm.

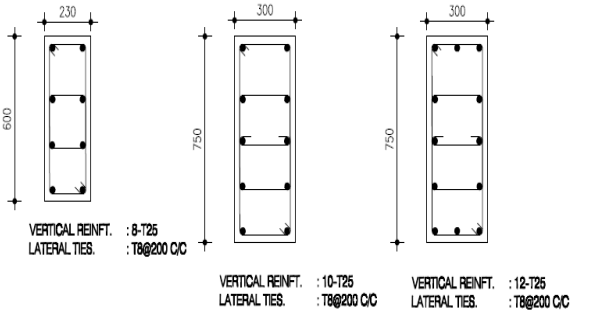

Fig. 2. Column Reinforcement

A. Models Considered For The Analysis

Following four base models are analyzed using equivalent static analysis method and nonlinear static (Pushover Analysis) for seismic loads in X and Y direction.

- *Model 1: Bare Frame without diaphragm:* The weight of the masonry infill wall is considered as UDL on the beam and also for seismic mass calculation. The stiffness of the slab is not considered for the analysis. The weight of slab is considered on the beam and also seismic mass calculation.
- *Model 2: Bare Frame with Semi Rigid Diaphragm:* The weight of the masonry infill wall is considered as UDL on the beam and also for seismic mass calculation. The slab is considered as membrane with semirigid diaphragm.
- *Model 3: Bare Frame with Rigid Diaphragm:* The weight of the masonry infill wall is considered as UDL on the beam and also for seismic mass calculation. The slab is considered as membrane with rigid diaphragm.
- *Model 4: Bare Frame with Shell:* The weight of the masonry infill wall is considered as UDL on the beam and also for seismic mass calculation. The slab is considered as infinitely

B. Structural Modelling

The building is modeled and analyzed for static, loads due to predominant mode of vibration and pushover analyses, using the finite element package ETABS. The mass of the slab was lumped at the centre of mass location at each floor level. Design lateral forces at each storey level were applied at the centre of mass locations independently in two horizontal directions (*X*- and *Y*- directions). Lateral load calculation and its distribution along the height have been manually verified. Beams have moment (M3) hinges, whereas columns have axial load and biaxial moment (PMM) hinges. The displacement controlled pushover analysis was monitored up to displacement equal to 4% of the height of the RC frame. The geometric nonlinearity effects were also considered for the analysis.

IV. Result And Discussion

Linear static, loads due to predominant modes of vibration and pushover analysis is conducted on four models for seismic loads defined as per IS 1893-2002 (Part-I) using ETABS. The pushover analysis provides an insight into the structural aspects, which control the performance during earthquakes. It also provides data on the strength and ductility of a building. The results obtained from analysis are tabulated in Table-1 and compared and discussed.

TABLE I.
PERFORMANCE POINTS OF DIFFERENT DIAPHRAGMS FOR DIFFERENT PUSHOVER LOAD

Type of Pushover Load	**Type of RC Frame**	**Bare Frame**	
		Performance Point(V,d)	***Performance Point(Sa,Sd)***
Static EQ-X	WithoutDiaphragm	(1322.567,0.228)	(0.086,0.165)
	Semirigiddiaphragm	(1265.433,0.227)	(0.087,0.163)
	Rigid Diaphragm	(1359.031,0.228)	(0.094,0.162)
	With Shell	(1834.094,0.205)	(0.122,0.153)
Static EQ-Y	Without Diaphragm	(951.682,0.278)	(0.058,0.222)
	Semirigiddiaphragm	(912.83,0.277)	(0.058,0.221)
	Rigid Diaphragm	(N.A)	(N.A)
	With Shell	(1586.544,0.289)	(0.098,0.227)
RS-MODE-3	Without Diaphragm	(1092.418,0.278)	(0.070,0.212)
	Semirigiddiaphragm	(1097.351,0.267)	(0.074,0.203)
	Rigid Diaphragm	(1347.616,0.214)	(0.090,0.162)
	With Shell	(1894.826,0.218)	(0.122,0.169)
RS-MODE-1	Without Diaphragm	(N.A)	(N.A)
	Semirigiddiaphragm	(N.A)	(N.A)
	Rigid Diaphragm	(898.745,0.271)	(0.056,0.225)
	With Shell	(1690.952,0.263)	(0.101,0.213)

According to the Fig. 3- Fig. 4, RC Frame with slab modeled as a shell element is showing more than 40% better performance in terms of base shear but weak in showing the ductile behavior when compared to other models. This may be because slab behaves monolithically with beam and adds additional stiffness and strength to the beam; hence loads are concentrated in the ground storey and exhibits soft storey effect where as in RC frame without diaphragm the horizontal loads are distributed throughout the height. There no much significant variation in performance in RC frame when the slab modeled as membrane with semirigid diaphragm and without any diaphragm

V. Conclusion

- RC frame with slab as shell element showed better performance than frame without diaphragm, with semirigid and rigid diaphragm in terms of base shear in transverse and longitudinal direction.
- Failure Mechanism in RC frame with slab as shell element is concentrated only in the ground floor but in case of frame without diaphragm, semi rigid and rigid diaphragm it is distributed throughout the height.

Acknowledgment

The authors would like to express their sincere thanks to The Director, and H.O.D, Civil engineering, Manipal Institute of Technology, Manipal for providing necessary facilities required for the present study.

References

[1] ATC-40,"Seismic evaluation and retrofit of concrete buildings". Report ATC-40, Applied Technology Counci;2000.

[2] FEMA-273, NEHRP guidelines for the seismic rehabilitation of buildings, Federal Emergency Management Agency, Washington, DC;1997.

[3] IS 1893 -part 1,"Provision on Seismic Design of Buildings", Bureau of Indian Standards, New Delhi;2002.

[4] G.Uva, D.Raffaele, F.Porco, A.Fiore." On the role of equivalent strut models in the seismic assessment of infilled RC buildings.Engineering Structure;vol 42,May 2012:pp83-94.

[5] Mehmet Inel and Hayri Bayton Ozmen."Effects of plastic hinges properties in nonlinear analysis of reinforced concrete buildings. Engineering Structure";vol 28,March 2006:pp1494-1502.

[6] P.Poluraju, P.V.S Nageswara rao."Pushover analysis of reinforced concrete frame structure using SAP 2000". International Journal of Earth Sciences and Engineering;vol 4,Oct 2011:pp684-690.

[7] R.S.Deshpande, A.B Surekha, "Seismic Analysis of RC Frame Building with Soft First Storey", Proceedings of the Seventh StructuralEngineeringConvention,AnnamalaiUniversity,Annamalainagar, T.N.,India,2010.

[8] KiranKamath, B.S Spoorthi, A.RAvinash and BalakrishnaRao, "Response of RC Frame Building with Varying Soft Storey Subjected to Seismic Loading", National Conference on Contemporary Civil Engineering Research & Practices, Manipal Institute of Technology, Manipal,April 2012.

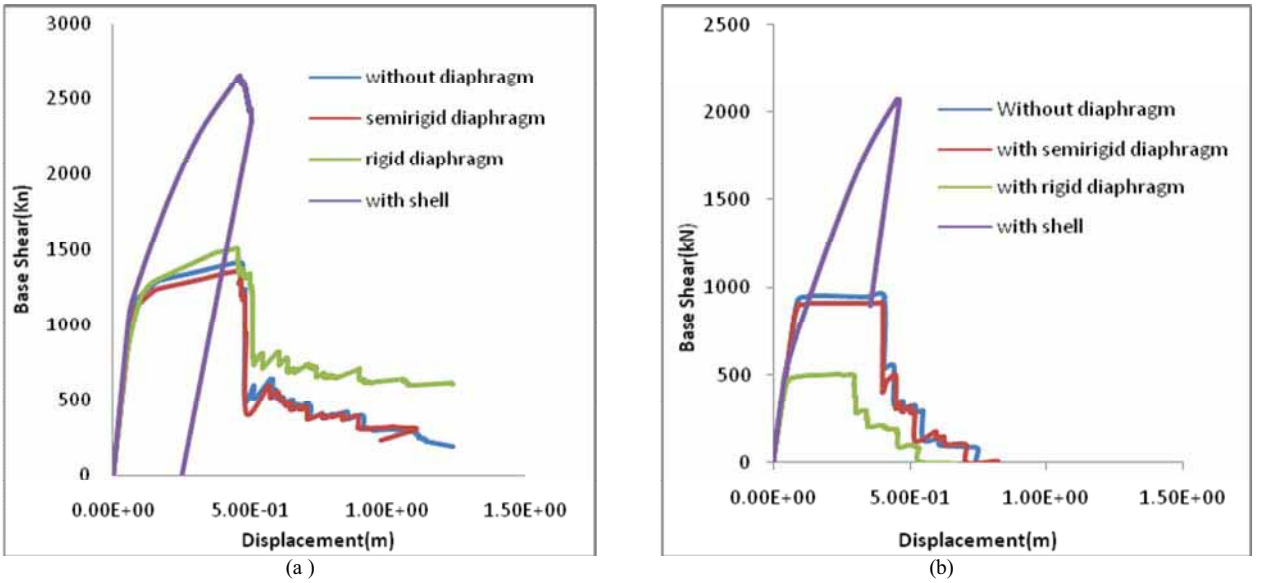

(a) (b)

Fig.3. Evaluating the Performance of the BareFrame for different diaphragms: (a) Static Pushover Load in EQX , (b) Static Pushover Load in EQY

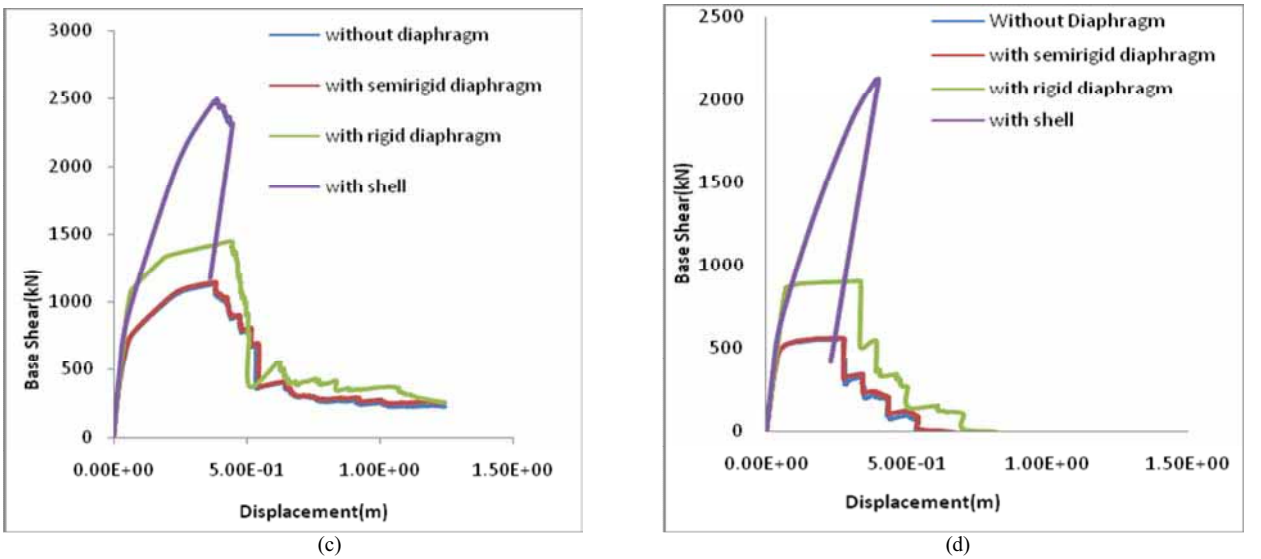

(c) (d)

Fig.4. Evaluating the Performance of the BareFrame for different diaphragms: (c) Response Spectrum Load –Mode3 (d) Response Spectrum Load –Mode-1

Electronic System Level Validation of QinQ and IPinIP Tunnel (L2/L3 tunnel) in Ethernet Switch

Dhanya K.N[#1], K Rajesh Shetty[*2]

[#]*M.Tech Student, Dept of E&C, NMAMIT, Nitte*
[1]dhanya_kodthuguly@yahoo.com

[*]*Associate. Prof., Dept of E&C, NMAMIT, Nitte.*
[2]krshetty_nitte@ yahoo.co.in

***Abstract*— Validation is one of the most complex and expensive tasks in the current System on Chip (SoC) design process. As chip design complexity continues to increase, validation methodologies are becoming highly complicated task in the current state of the art SoC design process. Design at the Electronic System-Level (ESL) tackles the increasing complexity of embedded systems by raising the level of abstraction in system specification and modeling[11]. It comes in the initial stage of the chip design cycle. The paper explores Electronic System Level validation of Layer2 and Layer3 tunnel feature which is used for forwarding the packets in the network efficiently. Validation is done by developing test cases for the software code to be validated using a scripting language. Test cases are developed to cover all possible scenarios based on the customer requirement. This will ultimately help in providing a bug free L2/L3 feature software code for Register Transfer Level synthesis.**

***Keywords*— ESL, QinQ, IPinIP tunnel**

I. INTRODUCTION

Electronic System Level (ESL) validation is one of the most complex and expensive task in the current system on chip design process.ESL validation is the task to validate ESL designs at higher abstraction level. It is the task to validate a model that represents hardware above RTL (Register Transfer Level) abstract level. System validation challenges have gone beyond the scope of what RTL can address. The main goal for high level synthesis tools is to map the high level specification correctly to RTL. If there is any dead code, or incorrect specifications, high level synthesis tools cannot identify that. RTL verification will detect dead code or incorrect specifications, but forces the user to go back to the high level model, make the modifications and run the synthesis again. Each synthesis run takes time, which could be avoided if dead code or incorrect specifications could be detected in the high level model. Electronic System Level validation or High level model validation reduces the number of design iterations, saves time and overhead costs. ESL design methodologies have been enabled by automation and tools for analysis, synthesis and validation of SoCs from models specified at higher levels of abstractions than RTL. One of the cornerstones of ESL design is the creation of optimized hardware from high-level specifications using High Level Synthesis (HLS). The HLS enable automated generation of RTL hardware from the software code. The benefits of using HLS are twofold: faster RTL creation and reduced verification/debugging effort since the RTL is created using an automated flow. ESL methodology is used for development and testing an Ethernet Switch which supports Layer 2 switching, Layer 3 routing. After more than a decade of research and development, ESL techniques have seen widespread adoption in a variety of SoC design activities [2].

The QinQ tunneling features, a L2 tunnel, enable the service providers to use a single VLAN to support customers who have multiple VLANs. Customer VLAN IDs are preserved and traffic from different customers is segregated within the service-provider infrastructure even when they appear to be on the same VLAN. The QinQ tunneling expands VLAN space by using a VLAN-in-VLAN hierarchy and tagging the tagged packets. A port configured to support QinQ tunneling is called a tunnel port. When tunneling is configured, a tunnel port is assigned to a VLAN that is dedicated to tunneling. Each customer requires a separate VLAN, but that VLAN supports all of the

customer's VLANs. An IP tunnel is an Internet Protocol (IP) network communications channel between two networks. It is used to transport another network protocol by encapsulation of its packets.

II. Validation Design

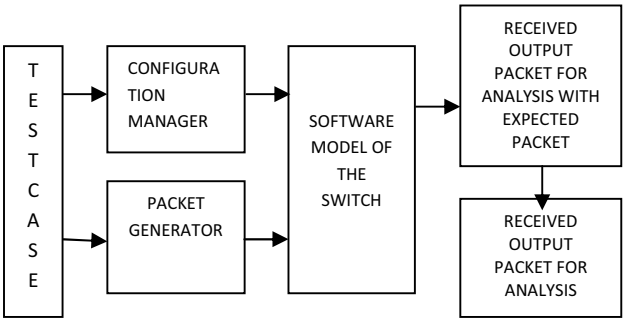

Fig. 1: Software Validation Model

Software model of a chip is kept in place of an emulation board as shown in figure 1. Controlled set of IPv4/IPv6 packets are sent into the software model using a packet generator. All the entry table, registers, ports, VLAN entries etc., related to the switching configurations for validation of the software model is hand coded in bit level into the software model using configuration manager. The packets received from the output ports of the software model of the chip are compared with the expected packet for correctness. Expected packet is the expected behavior of the software model with respect to the transmitted packet and the switching configurations within the software model of the chip. If the expected packet and the received packet match then it is concluded that block of software model which has been validated is working as per its intent.

Packet Generator generates and also traps the packet. It is virtually written using high level programming language. It simulates the behavior of Ixia chassis to generate as well to process the thousands of packets at very high speed to test multilayer gigabyte Ethernet switches. The packet size starts with 64 bytes to 1.5 Mb. The transmitted packets from the Packet Generator is analyzed and accepted by the model.

Test cases for validation of the Software Model can be developed using any scripting language. The Transmitting packets, Receiving packets and the configurations that has to be dumped into the software model of the switch are all configured in the test case. All possible scenarios in the Software Model are taken in consideration and test case is developed for all the scenarios. Dropped packets are sent to the CPU for further processing. The Interface which generates the received output from the Software Model is then matched with the expected output of the model to validate its correctness. Peripheral Component Interconnect Device is an industry specification for interconnecting certain computer hardware components. It is used to interconnect the Packet Generator, Software Model and the Configuration Manager Interface.

III. Double VLAN Tagging (QinQ)

A. Implementation

IEEE 802.1QinQ is an Ethernet networking standard for Ethernet frame formats. The technique is also known as provider bridging, Stacked Virtual Local Area Networks (VLANs) or simply QinQ or Q-in-Q. QinQ allows multiple VLAN headers to be inserted into a single frame, an essential capability for implementing Metro Ethernet network topologies. 802.1QinQ specifies architecture and bridge protocols to provide separate instances of the MAC services to multiple independent users of a Bridged Local Area Network in a manner that does not require cooperation among the users, and requires a minimum of cooperation between the users and the provider of the MAC service [1].

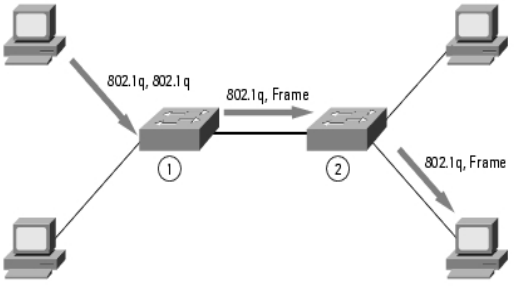

Fig. 2: Double VLAN (QinQ) Tagging scenario

QinQ adds a second 802.1q VLAN ID (VID) so that the original customer VID can be carried transparently across the (Wide Area Network) WAN, and the Service Provider VID can be used to separate customers. The original 12 bit VLAN address space of 802.1q is maintained, so that more than 4096 service instances cannot be supported. This limits the usefulness of the technology. Encapsulating IEEE 802.1q VLAN tags within 802.1q enables service providers to use a single VLAN to support customers who have multiple VLANs as shown in figure 2. The IEEE 802.1QinQ VLAN Tag Termination feature on the sub interface level preserves VLAN IDs and keeps traffic in different customer VLANs segregated. This enables for customers to run their own VLANs inside

VLAN provided by service provider. This way the service provider can just configure one VLAN for the customer and customer can then treat that VLAN as if it was a trunk.

B. QinQ Frame format

Fig. 3: Double VLAN Tag (QinQ) format

802.1ad has a 12-bit Virtual Local Area Networks Identification (VLAN ID) field, which has a theoretical limit of 212 =4096 tags. With the growth of networks, this limitation has become more acute. A double-tagged frame has a theoretical limitation of 4096×4096=16777216, sufficient to accommodate network growth for the next several years. The addition of a second tag allows operations that would have the VLAN ID field simply been expanded from 12 bits to 24 bits (or any other large value) as shown in figure 3. Having multiple tags—the tag stack—allows switches to more easily modify frames. In a tag stack scheme, switches can add ("push"), remove ("pop") or modify single or multiple tags. A multi-tagged frame not only has multiple VLAN IDs, but has multiple Ethertypes and other VLAN header bit fields [4].

C. Advantages over single VLAN tagging

1) In QinQ, an extra tag increases the number of VLANs to 4096×4096=16777216 vlans.Hence double tagging increases the vlan space.

2) Double tagging enables Transparent and Mapped services (VLAN Translation) for a Service provider.

3) Shield the VLAN ID of the user, so as to save the public network VLAN ID resource of the service provider.

4) The user can plan the private network VLAN ID, avoiding the confliction with the public network and other user VLAN IDs.

5) Provide the simple L2 VLAN solution.

IV. IPinIP TUNNELING

Tunneling is a technique for establishing point-to-point tunnels by encapsulating packets within IPv4 headers to carry them over IPv4 routing infrastructures and encapsulating packets with IPv6 headers to carry then over IPv6 routing infrastructures shown in figure 4. IP tunnels are often used for connecting two disjoint IP networks that does not have a native routing path to each other, via an underlying routable protocol across an intermediate transport network. In IP tunneling, every IP packet, including addressing information of its source and destination IP networks, is encapsulated within another packet format native to the transit network. The key to a successful IPv6 transition is compatibility with the large installed base of IPv4 hosts and routers [8]. Maintaining compatibility with IPv4 while deploying IPv6 will streamline the task of transitioning the Internet to IPv6.

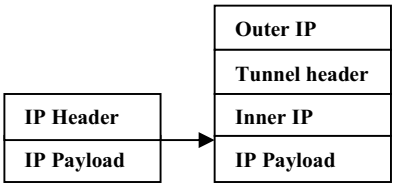

Fig. 4: IPinIP tunneling

A .TTL rule

When encapsulating a datagram, the TTL in the inner IP header is Decremented by one if the tunneling is being done as part of forwarding the datagram; otherwise, the inner header TTL is not changed during encapsulation. The TTL in the inner IP header is not changed when decapsulating. If, after decapsulation, the inner datagram has TTL = 0, the decapsulator must discard the datagram.

B. Routing failure

When a datagram arrives at a router for forwarding and the router determines that the datagram has to be encapsulated before further delivery. If the IP Source address of the datagram
matches the IP address of the tunnel destination, the router must not tunnel the datagram and it should be discarded.

C. ICMP messages

ICMP messages indicating an error in processing a datagram include a copy of (a portion of) the datagram causing the error. After an encapsulated datagram has been sent, the encapsulator may receive an ICMP message from any intermediate router within the tunnel other than the tunnel exit point. The action taken by the encapsulator depends on the type of ICMP message received [9].

D. Tunnel management

The encapsulator uses the ICMP messages received from the interior of a tunnel to update the soft state information for that tunnel. By maintaining "soft state" about tunnels the encapsulator can return accurate ICMP messages to the original sender.

V. Test Scenarios And Results

A. QinQ action

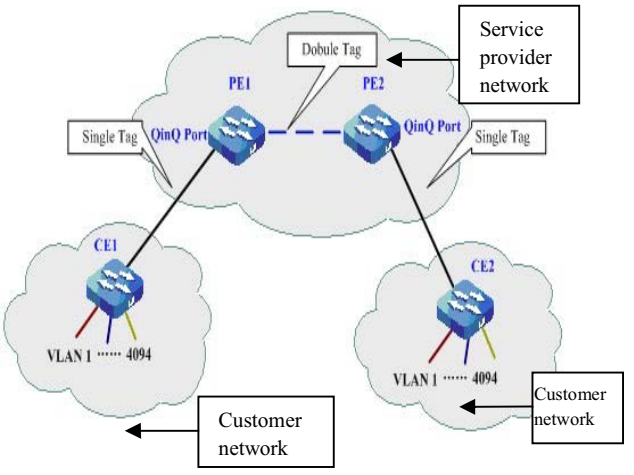

Fig. 5: QinQ Tagging Scenario

The upstream packet of the CE1 switch carries one layer of VLAN tag shown in figure 5. The packet reaches the QinQ port of the PE1 switch. According to the configuration of the QinQ port, add one out layer of VLAN TAG to the packet. The packet with two layers of VLAN tags is forwarded to PE2 via the public network. On the QinQ port of PE2, the out layer of VLAN TAG is deleted, and the packet recovers to have one layer of VLAN Tag and is forwarded to CE2.

B.Customer packet (untag) from CE1 to PE1

CUSTOMER TAG ACTION	SERVICE PROVIDER TAG ACTION	RECEIVED PACKET
NOP/Replace/ Delete	Add	Single tagged packet[PVID]
Add	Add	Double tagged packet[PVID,NCVID]

C. Customer packet (ptag) from CE1 to PE1

CUSTOMER TAG ACTION	SERVICE PROVIDER TAG ACTION	RECEIVED PACKET
NOP	Add	Double tagged packet[PVID,0]
Replace	Add	Double tagged packet[PVID,NCVID]
Delete	Add	Single tagged packet[PVID]
Add	Add	Double tagged packet[PVID,0]

D.Customer packet (stag) from CE1 to PE1

CUSTOMER TAG ACTION	SERVICE PROVIDER TAG ACTION	RECEIVED PACKET
NOP	Add	Double tagged packet[PVID,CVID]
Replace	Add	Double tagged packet[PVID,NCVID]
Delete	Add	Single tagged packet[PVID]
Add	Add	Double tagged packet[PVID,CVID]

E.Single tagged/double tagged Packet from PE2 to CE2

SERVICE PROVIDER PACKET	SERVICE PROVIDER TAG ACTION	CUSTOMER TAG ACTION	RECEIVED PACKET
Single tagged packet[PVID]	Delete	INVALID	Untagged packet
Single tagged packet[PVID]	Delete	Add	Single tagged packet[NCVID]
Single tagged packet[PVID]	Replace	INVALID	Single tagged packet[NCVID]

SERVICE PROVIDER PACKET	SERVICE PROVIDER TAG ACTION	CUSTOMER TAG ACTION	RECEIVED PACKET
Double tagged packet[PVID,CVID]	Delete	NOP	Single tagged packet[CVID]
Double tagged packet[PVID,CVID]	Delete	Replace	Single tagged packet[NCVID]
Double tagged packet[PVID,CVID]	Delete	Delete	Untagged packet
Double tagged packet[PVID,0]	Delete	NOP	Priority tagged packet
Double tagged packet[PVID,0]	Delete	Replace	Single tagged packet[NCVID]
Double tagged packet[PVID,0]	Delete	Delete	Untagged packet
Double tagged packet[PVID,CVID]	Replace	Delete	Single tagged packet[NCVID]

F.Tunnel encapsulation

Encapsulate an IP datagram using IP in IP encapsulation, an outer IP header is inserted before the datagram's existing IP header. The outer IP header Source Address and Destination Address identify the endpoints of the tunnel. The inner IP header Source Address and Destination Addresses identify the original sender and recipient of the datagram, respectively. Test cases are developed to cover all the scenarios in 6 over 4 tunnel network.

TEST SCENARIO	TRANSMITTED PACKET	RECEIVED PACKET
6in4 Tunnel for unicast packet	IPv6 unicast packet	Tunneled packet with outer header as IPV4 and inner header as IPv6.
6in4 Tunnel Initialization for multicast packet	IPv6 multicast packet	Tunneled packets with outer header as IPV4 and inner header as IPv6 on multiple ports.

G.Tunnel decapsulation

When a router receives an IP datagram that is addressed to one of its own IP addresses or a joined multicast group address, and the value of the protocol field is 41, then the packet is a tunnel packet and should belong to one of the configured tunnel interfaces by checking source/destination addresses, reassembled and remove the outer IP header resulting in an single IP header with datagram.

TEST SCENARIO	TRANSMITTED PACKET	RECEIVED PACKET
6in4 Tunnel Termination for unicast packet	Tunneled packet with outer header as IPV4 and inner header as IPv6	IPv6 unicast packet
6in4 Tunnel Termination for multicast packet	Tunneled multicast packet with outer header as IPV4 and inner header as IPv6	IPv6 packets on multiple ports with outer IPv4 header removed.

H. Drop scenario

Test case for different scenarios where the packets could not be forwarded further that could be encountered in the network for any tunneling.

TEST SCENARIO	TRANSMITTED PACKET	RECEIVED PACKET
Terminating a tunnel with inner/outer Destination IP (DIP)=0	Tunneled 6in4/4in6/4in4/6in6 packet with DIP=0	Packet will be Dropped/ Copied to CPU as Destination IP address is invalid.
Terminating a tunnel with inner/outer DIP=SIP	Tunneled 6in4/4in6/4in4/6in6 packet with DIP=SIP	Packet will be Dropped/ Copied to CPU as Destination IP address is equal to source IP address.
Terminating a tunnel with	Tunneled 6in4/4in6/4in4/6in6 packet with SIP=0	Packet will be Dropped/ Copied to

inner/outer SIP=0		CPU as address is invalid.
Initializing a tunnel when TTL=0	IPv4/IPv6 packet with TTL value 0.	Packet will be Dropped/Copied to CPU as the TTL value in the IP header has expired.
Terminating a tunnel when outer TTL=0	Tunneled packet with outer header TTL value 0.	Packet will be Dropped/Copied to CPU while tunnel termination as the TTL value in the outer IP header has expired
Terminating a tunnel when inner TTL=0	Tunneled packet with inner header TTL value 0.	Packet will be Dropped/Copied to CPU during forwarding as the TTL value in the inner IP header has expired.

VI. CONCLUSION

ESL validation is one of the most efficient and time saving method of validating a chip during its design cycle. There are fewer things to verify, fewer lines of code to debug, higher simulation performance, and quicker fixes and most importantly time to market for a chip will be reduced.

QinQ extends the benefits of VLAN technology beyond the boundary of Ethernet LANs. It maintains the simplicity and cost of ownership advantages of Ethernet, while expanding its scalability and geographical reach. The use of QinQ technology enriches the application scenarios of VLAN. As the metro Ethernet develops, QinQ plays an increasingly important role in the metro Ethernet solutions due to the following reasons like simplicity, flexibility and support for a wide variety of services.

It is highly dependent on Network Layer features IPv4, IPv6, L3 MPLS and IP Tunneling to enable reliable and secure communication of voice, video and data traffic on a single high-performance network. The switch has been extensively validated during ESL Validation phase.

REFERENCES

[1] Broadcom Corporation, "*A Scalable Approach to Gigabit Ethernet Switch Design*", Irvine, California, 2002.

[2] Cisco Systems, Inc "*Gigabit Multilayer Switching for the Campus*", 1998.

[3] Tony Jeffree, Mick Seaman, Stephen Haddock, "*IEEE Standard for Local and metropolitan area networks, Amendment 4: Provider Bridges*" IEEE Std 802.1ad™-2005 IEEE LAN/MAN Standards Committee New York, USA, 2006.

[4] Steve M. Mills, Richard H. Hulett, Judith Gorman, "*IEEE Standards for Local and metropolitan area networks Virtual Bridged Local Area Networks*" IEEE Std 802.1Q™, 2005 Edition, IEEE LAN/MAN Standards Committee, New York, USA, 2005.

[5] Huawei Technologies Co. Ltd. "*Technical White Paper for QinQ*", 2007.

[6] Cisco Systems, Inc., "*Virtual LAN Security Best Practices*", 2002.

[7] J. Postel, "Internet Protocol: DARPA Internet Program Protocol Specification," RFC 791, Sept. 1981.

[8] S. Deering, R. Hinden, "*Internet Protocol, Version 6 (IPv6) Specification*", RFC 2460, Dec. 1998.

[9] C.Perkins, "*IP Encapsulation within IP*", RFC 2003, Oct. 1996.

[10] E.Nordmark, R.Gilligan, "*Basic IPv6 Transition Mechanism*", RFC 4213, Oct. 2005.

[11] Tor Jeremiassen, Tim Kogel, Andres Takach, Grant Marti, Adam Donlin, Karam Chatha ,"*From ESL 2010 to ESL 2015",* Scottsdale, Arizona, USA, 2010.

[12] Rich Seifert, Wiley Pvt Ltd., "*The Switch Book: The Complete Guide To LAN Switching Technology*", 2002.

Microcontroller Based PWM Controlled Three Phase Four Switch Induction Motor Drive

Mr. Ravindra Keni[#1] Dr. Vinayak N. Shet[*2]
[#]*M.E Student, GEC Farmagudi.Goa*
[1]rmk_keni@yahoo.com
[*]*Head of Electrical and Electronics Engineering, Government Engineering Collage Farmagudi, Goa*

Abstract- **Microcontroller based PWM controlled four switch three phase inverter (FSTPI) fed Induction Motor drive. The advantage of this inverter that uses of 4 switches instead of conventional 6 switches is lesser switching losses, lower electromagnetic interference (EMI), less complexity of control algorithms and reduced interface circuits. Simulation is carried out using MATLAB SIMULINK and in the experimental work a prototype model is built to verify the simulation results. PIC microcontroller (PIC 16F877A) is used to generate the PWM pulses for FSTPI to drive the 0.5 hp 3-phase Induction Motor.**

Keywords- *Four Switch Three Phase Inverter (FSTPI), Induction Motor (IM), Pulse Width Modulation (PWM), Total Harmonic Distortion (THD), Peripheral Interface Controller (PIC).*

I. INRODUCTION

Induction motor (IM) has been utilized as a workhorse in the industry due to its easy construction, high robustness, and generally satisfactory efficiency. With the invent of high speed power semiconductor devices three-phase inverters play the key role for variable speed ac motor drives. Traditionally, 6-switch, 3-phase (6S3P) inverters have been widely utilized for variable speed IM drives. This involves the losses of the six switches as well as the complexity of the control algorithms and interface circuits to generate six PWM logic signals [1][2].

In the past, researchers mainly concentrated on the development of the efficient control algorithms for high performance variable speed IM drives. However, the cost, simplicity and flexibility of the overall drive system which become some of the most important factors did not get that much attention to the researchers. That is why, despite extensive research in this area most of the developed control system failed to attract the industry. Thus, the main issue of this project is to develop a cost effective, simple and efficient high performance IM drive[1]. Usually, high performance motor drives used in robotics, rolling mills, machine tools, etc. require fast and accurate response, quick recovery of speed from any disturbances and insensitivity to parameter variations.

A cost effective 4S3P inverter fed IM drive is developed and successfully implemented in real-time for a prototype 0.5 hp squirrel cage induction motor. The 4 switches make the inverter drive less costly, less switching losses, less chances of destroying the switches due to lesser interaction among switches, less complexity of control algorithms and interface circuits as compared to the conventional 6S3P inverter. Furthermore, the proposed control approach reduces the computation for real-time implementation. The performance of the proposed drive is investigated both theoretical and experimentally at different operating conditions.A performance comparison of the proposed 4-switch 3-phase inverter fed drive with a conventional 6-switch, 3-phase inverter fed drive is also made in terms of total harmonic distortion (THD) of the stator current and speed response [3]. The proposed inverter fed IM drive is found acceptable considering its cost reduction and other advantageous features mentioned earlier.

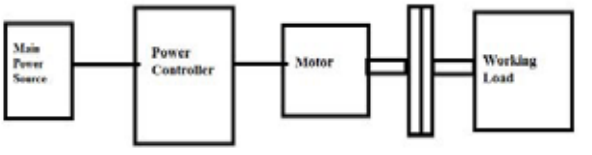

Fig. 1 Electric Drive System

Induction motors are being used for many industrial and commercial applications because it its easy build, high robustness, and generally satisfactory efficiency. AC induction motors, which contain a cage, are very popular in variable-speed drives. They are simple, rugged, inexpensive and available at all power ratings. Progress in the field of power electronics and microelectronics enable the application of induction motors for high-performance drives. The speed of the induction motor can be controlled by varying its input AC voltage and frequency using an Inverter. A standard six switch three phase voltage source inverter has six switches in three legs with a pair of complementary power switches per phase. A reduced

switch count voltage source inverter i.e. four switch three-phase inverter (FSTPI)] uses only two legs, with four switches. The advantage of this inverter due to the use of 4 switches instead of conventional 6 switches is lesser switching losses, lower electromagnetic interference (EMI), less complexity of control algorithms and reduced interface circuits. The four-switch inverter topology is attractive cost wise when it is compared with conventional six-switch voltage source inverters. In the four-switch inverter, one motor terminal is connected to the centre tap of the dc-link capacitors.

II. PROBLEM STATEMENT

However, four-switch inverters are known to have several disadvantages compared to normal six-switch inverters: the voltage utilization factor is halved compared to the six-switch inverter. Specifically, the peak phase voltage of the four-switch inverter is, while that of six-switch inverters is $V_{dc}/ (2 \sqrt{3})$. While that of six switch inverter is $V_{dc} / \sqrt{3})$. On the other hand, capacitor centre tap voltage is fluctuating, and it destroys the balance among the motor phase currents. The reason for this is that current flow through a capacitor either increases or decreases the voltage steadily for each half cycle. Therefore, the voltage fluctuation increases as the load torque becomes higher or the frequency becomes lower. The unbalanced motor current leads to an inverter failure and torque pulsation [1].

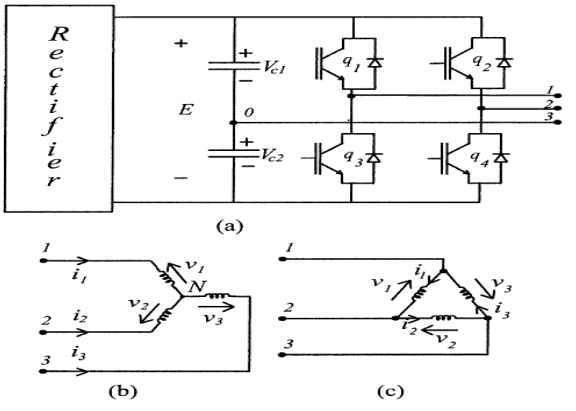

Fig.2 Ac drive system configuration.

Fig. 2 Ac drive system configuration [3]. The influence of different switching patterns on outputvoltage symmetry, current waveform, switching frequency andcommon mode voltage is examined. The paper also discusseshow the use of the Wye and delta connections of the motor windings affects the implementation of the pulse width modulator. The utilization of an induction motor, with its windingsconnected in delta is studied here as the dc-link voltage used, in respect to the Wye connection. For alternative to reducethe Wye connection it is investigated, how the common-modevoltage can be reduced. The reduction of the common modevoltage permits to mitigate effects of common mode currents,which commonly are responsible for damage of motor bearingsand bearing lubrication [1].

Thispaper presents a general method to generate pulse width modulated (PWM) signals for control of four-switch, three phase voltage source inverters, even when there are voltage oscillations across the two dc-link capacitors.

With respect to the circuit shown in Fig. 2(a) it is assumed that the conduction state of the power switches is associated with binary variables 1 to 0. Therefore, a binary "1" will indicate a closed switch, while "0" will indicate the open state. Pairs q1-q3 and q2-q4 are complementary and, as a consequence,q3=1-q1 and q4=1-q2. Also it will beassumed that a stiff voltage is available across the two dc-link capacitors, and Vc1=Vc2=Ē/2 , where Ē corresponds to a stiff dc-link voltage, i.e., the actual value of the dc-link voltage Ē.

The details of the components used in this experiment are given in Table 1. The potential transformer is used to provide the power to microcontroller board and driver circuit board. A single phase diode bridge rectifier and filter circuit is used to convert AC to DC. Four MOSFETs and 2-split capacitors are used to form FSTPI. The output of FSTPI is connected to the 0.5 hp 3-phase Induction Motor. Oscilloscope is used to display the PWM pulses and the output current waveform of i_a, i_b, i_c,[1][3].

The power circuit of the FSTPI fed drive is shown in fig. 3, the Circuit consists of 4 switches S_1 S_2 $S_3$and S4 and split capacitors C_1 and C_2. The 3-Phase AC input. Which is of fixed frequency, is rectified by the rectifier switches. The power circuit is the three phase four switch inverter. Two phases 'a' and 'b' are connected to the two legs of the inverter, while the third phase 'c' is connected to the centre of the dc-link capacitor C_1 and C_2[4].

The 4 power switches are denoted by the binary variables S_1 to S_4, where the binary '1' corresponds to an On state and binary '0' corresponds to an Off state. The states of the upper switches (S_1, S_2) and lower switches (S_3, S_4) of a leg are complementary that is $S_3 = 1 - S_1$ and $S_4 = 1 - S_2$ the terminal voltages V_{as}, V_{bs}

and V_{cs} of a 3 phase Y connected induction Motor can be expressed as the function of the states of the upper switches as follows

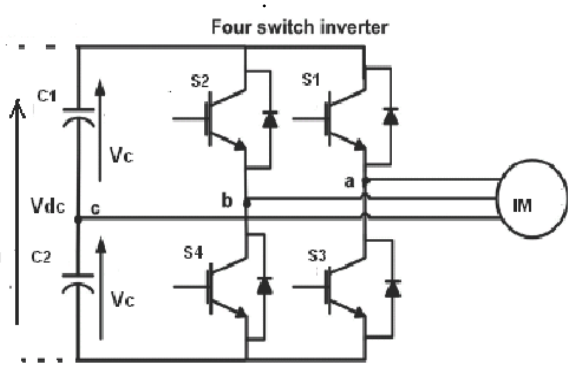

Fig. 3. Four Switch Three Phase Inverter.

$$Vas = \frac{Vc}{3}\ (4 * S1 - 2 * S2 - 1\ )(1)$$

$$Vbs = \frac{Vc}{3}\ (-2 * S1 + 4 * S2 - 1)(2)$$

$$Vcs = \frac{Vc}{3}(-2 * S1 - 2 * S2 + 2\ )(3)$$

Where V_{as}, V_{bs}, V_{cs} are the inverter output voltages V_c is the voltage across the dc link capacitors V_{dc} is the voltage across the capacitors C_1 and C_2(V_{dc} = V_c/2) [5].

The following table 1 shows the different modes of operation and the corresponding output phase voltages of the inverter.

TABLE 1
SWITCHING AND OUTPUT PHASE VOLTAGES

Switching Status		Output Voltages		
S1	S2	Vas	Vbs	Vcs
0	0	-V_c/3	-V_c/3	2V_c/3
0	1	-V_c	V_c	0
1	0	V_c	-V_c	0
1	1	V_c/3	V_c/3	-2V_c/3

The microcontroller based control system hardware has been programmed to vary the frequency of the PWM signal that controls the frequency of the FSTPI. The PWM module gets two inputs duty cycle and frequency. The frequency is configurable within the range 20Hz – 2 kHz and the duty cycle can be varied from 0% to 100%. The PWM signals of the MCU are applied to the gate of MOSFET through gate driver circuit. The gate driver provides isolation, low impedance and high current supply to drive the MOSFET. By controlling the input voltage to the analog ADC, the output frequency of the Microcontroller can be controlled.

III. PERFORMANCE INDICES

The details of the components used in this experiment are given in Table 2 The potential transformer is used to provide the power to microcontroller board and driver circuit board. A single phase diode bridge rectifier and filter circuit is used to convert AC to DC. Four MOSFETs and 2-split capacitors are used to form FSTPI. The output of FSTPI is connected to the 0.5 hp 3-phase Induction Motor. Oscilloscope is used to display the PWM pulses and the output current waveform of i_a i_b i_c.

TABLE 2

Hardware Components	
Components	**Ratings**
Capacitor	1000µf, 250V
Inverter	MOSFET (IRF 460)
Induction Motor	0.5 hp, 3 phase, 50Hz, 400V, 1430 rpm
Microcontroller	16F877A
Rectifier	110V, 5A, Single phase Bridge Rectifier

A. Generation of a Sinusoidal waveform

The easiest way to generate a sinusoidal waveform is to use a look-up table. You could also calculate the sine value on the fly, but it's just not worth spending the CPU time to do this. A look-up table is used that contains all the points of a sine wave. The sine values are read from the table at periodic intervals, scaled to match the allowable range of duty cycles, and then written to the duty cycle registers. A sine pointer variable is maintained in software that defines the present location in the table. This pointer has to be adjusted at periodic intervals, usually at the beginning of each PWM period. If a constant adjustment value is added to the pointer at each interval, the software will move through the table at a fixed frequency. The look-up table length is usually set to an even power of 2, such as 64, 128 or 256. This way, the software does not have to check the pointer value every time it is adjusted. The pointer can simply be allowed to roll over and reset to 0.

Assume that a 16-kHz PWM carrier is selected and the maximum modulation frequency is 60 Hz for a ACIM:

Number of the table Value = f_{pwm} / f_{modmax} ---- (1)
= 16000/60
=256

For this example, a 256 value sine table would be sufficient.

In practice, the code provided in this application note has 64 entry tables and provides good results.

B. Sine Table Pointer

Once the sine table size has been selected, the size of the sine table pointer variable can be chosen. Let's assume that a 256 value table is used for the sine values. At first glance, you might assume that an 8-bit pointer value would be sufficient. However, you will want the pointer value to be larger so that it will be easy to produce very low modulation frequencies. For the code examples in this application note, a 16-bit sine table pointer is used. The pointer represents a full 360 degrees of angle, where 0x0000 = 0 degrees and 0xFFFF = 359.9 degrees. Each time a new value is needed from the look-up table, the upper 8 bits of the pointer variable are used as the pointer index. The lower 8 bits of the pointer variable can be viewed as fractional bits.You will want to know the resolution of the modulation frequency. To find this resolution, you need to know how frequently the sine table pointer will be adjusted. For now, assume that this adjustment occurs every PWM period. Assuming a 16-kHz PWM frequency, the modulation frequency resolution would be:

$$\text{Mod Frequency Resolution} = f_{pwm}/2^{16} \quad \text{---} \quad (2)$$
$$= 0.244 \text{ Hz bit}$$

So this choice of resolution and PWM carrier frequency allows the modulation frequency to be adjusted in 0.244 Hz steps our variable speed application runs the motor at full speed with a modulation frequency of 60 Hz. To find the table pointer delta value that will provide a 60Hz modulation frequency.

$$f_{mod}/0.244 = 60/0.244 \text{ bit} \quad \text{---} \quad (3)$$
$$= 246 \text{ bits}$$

IV. PROBLEM FORMULATION

C. PWM generation in PIC microcontroller

8-bit PIC16F877A microcontroller was chosen to obtain the pulses for the FSTPI to drive the Induction Motor. This Microcontroller has a 25 MHz processor, 33 input/output (I/O) pins, interrupts, counters, timers, I/O ports, RAM, and ROM/EPROM. The peripheral interface controllers (PICs) are the integrated circuits based on CMOS technology. The main components of a PIC are RAM, EPROM, EEPROM, and Peripheral Interface Adaptor (PIA). These components are inserted in the same integrated circuit to reduce the size, the cost of the system and make design of the system easier. The address bus, the data bus and the control bus connecting the components are placed in the PIC circuit by the manufacturer. Because of these advantages, PICs have been preferred devices in practical control applications. PIC16F877A used in this work operates at 20 MHz clock frequency and runs each instruction as fast as 200 ns. Flash Program Memory is up to 8K×14 words. Data memory is partitioned into four banks which contain the General Purpose Registers and the Special Function Registers. Bits RP1 and RP0 are the bank select bits. Each bank extends up to 7Fh (128 bytes). It contains 1K EEPROM as a program memory, 15 special hardware registers, 36 general purpose registers and 64 byte EEPROM as a data memory. PICs have been preferred control devices because of their low cost, less energy consumption and small volume. The microcontroller has been programmed to vary the frequency of the PWM signal that controls the frequency of the voltage applied at the gate drives, and as a result of this the switching frequency of the inverter is controlled.

V. SIMULATIOM STUDY AND RESULTS

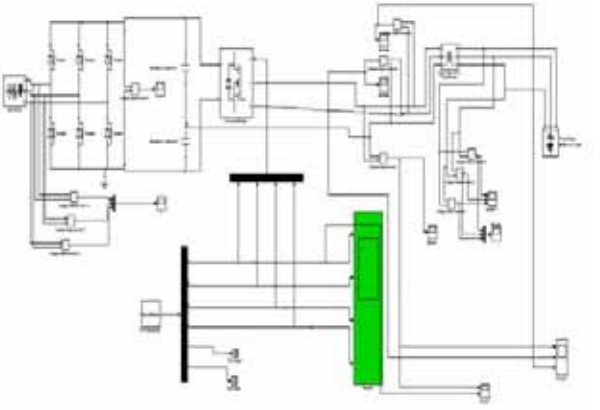

Fig. 4.Four Switch Three Phase inverter drive model

D. Circuit parameters

Vin = 400 V Phase to Phase rms Voltage

C1=C2= 1000 micro Farad

Modulation index =0.0 - 0.9

Switching Frequency = 0 - 2000 Hz

Ripple in the voltages across C1 and C2, The relation between the capacitors ripple voltages and the current in the capacitors is

$$ic = C\frac{\Delta Vc}{\Delta t}\ldots \quad (4)$$

$$C = ic\frac{\Delta t}{\Delta Vc} = \frac{ic}{\omega \Delta Vc} \quad (5)$$

The rated current is 1 A. the carrier is 4 kHz and supply voltage is 320 V, so the capacitor must be larger than

$$C \geq \frac{1}{4000*0.05*160} = 31.25\mu F \quad (6)$$

We used two 1000µF Capacitor in our experiment, because the capacitor has to supply start up current [5].

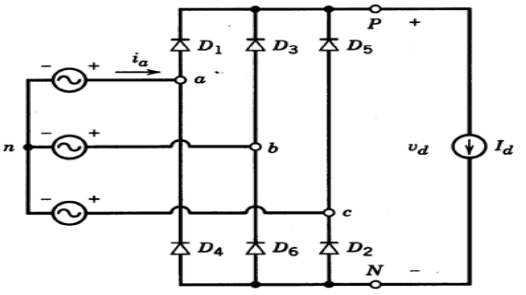

Fig. 5.Three Phase Full Bride Uncontrolled Rectifier

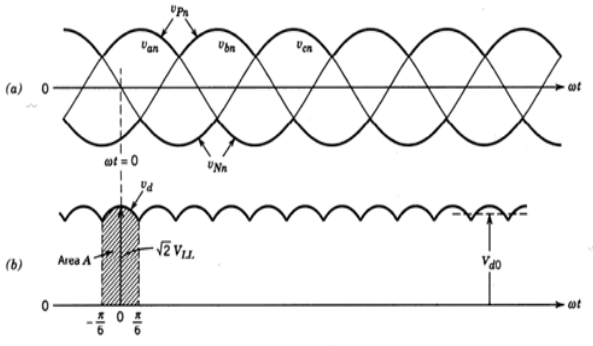

Fig. 6 Capacitor Voltage

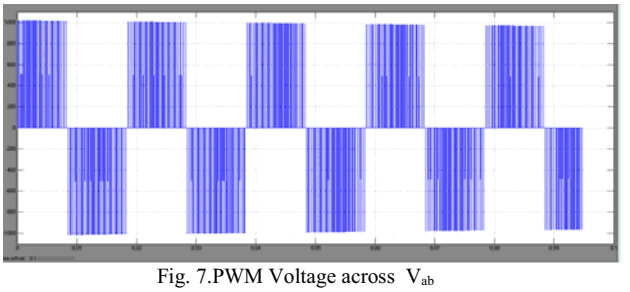

Fig. 7.PWM Voltage across V_{ab}

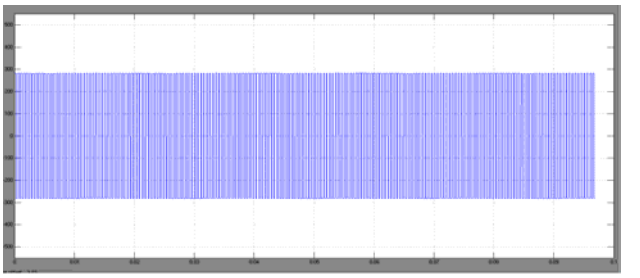

Fig. 8.PWM Voltage across V_{ac}

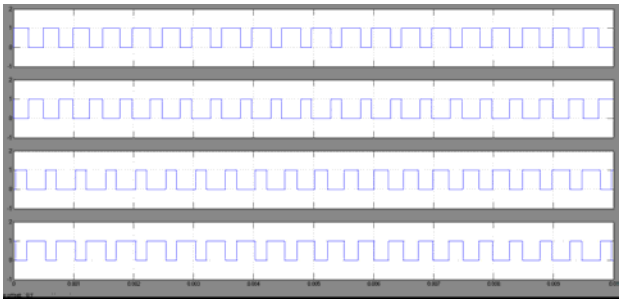

Fig. 9.Pulse applied to MosFET T1 through T4

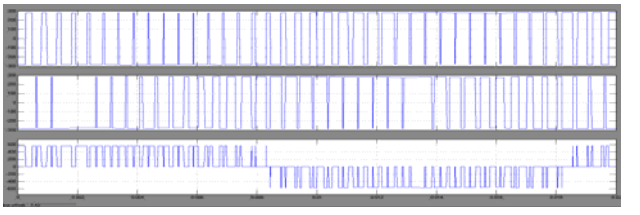

Fig. 10.Voltage Before Transformer

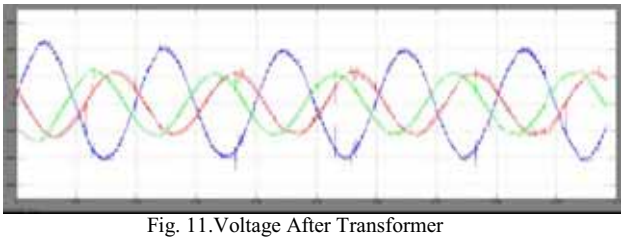

Fig. 11.Voltage After Transformer

VI. Conclusion

A PIC microcontroller based PWM controlled FSTPI fed Induction Motor drive has been designed and implemented successfully. The simulation and implementation results are presented to verify the feasibility of hardware the system. The implementation of the proposed work shows the practical industrial application FSTPI.

The MATLAB Simulation for TPFSIM is giving the three phase output shows, the motor input voltage is nearly three phase. The combination of PIC16 architecture and thoughtfully designed peripherals make the PIC16F877A an excellent choice for 3-phase

AC induction motor control applications. The PCPWM module provides sufficient PWM outputs and modes to directly drive a gate driver/inverter module, without the need of additional hardware to create complimentary channels or insert dead time. All of these features make it possible to design a wide range of powerful motorcontrol solutions with a minimum of parts.

VII. REFERENCES

[1] M.B.R. Correa, C.B. Jacobina, E.R.C. Silva*, A.M.N. Lima: A General PWM Strategy for* Four-switch Three-phase Inverters, IEEE Transactions on Power Electronics, Vol. 21, No. 6, Nov. 2006, pp. 1618 – 1627.

[2] M. N. Uddin, T. S. Radwana, and M. A. Rahman, "Performance analysis of a 4-switch, 3-phase inverter based cost effective IM motor drives," Electrical and Computer Engineering, Canadian Conference , pp. 85–88, 2004

[3] J. Kim*, J. Hong, K. Nam: A Current Distortion Compensation Scheme for Four-switch* Inverters, IEEE Transactions on Power Electronics, Vol. 24, No. 4, April 2009, pp. 1032 – 1040.

[4] Jin-Su Jang, Byoung-Gun Park, Tae-Sung Kim, Dong Myung Lee, Dong-Seok Hyun, "Sensor less Control of Four- switch Three-Phase PMSM Drive Using Extended Kalman Filter" IEEE, pp.1368-1372, June 2008.

[5] M.N. Uddin, T.S. Radwan, M.A. Rahman: Fuzzy-logic-controller-based Cost-effective Four-switch Three-phase Inverter-fed IPM Synchronous Motor Drive System, IEEE Transaction on Industry Application, Vol. 42, No.1, Jan/Feb. 2006, pp. 21 – 30.

[6] C.T. Lin, C.W. Hung, C.W. Liu: Position Sensor less Control for Four-switch Three-phase Brushless DC Motor Drives, IEEE Transactions on Power Electronics, Vol. 23, No. 1, Jan. 2008, pp. 438 – 444. *N.K. Mohanty, R. Muthu* 204

[7] F. Blaabjerg, D.O. Neacsu, J.K. Pedersen: Adaptive SVM to Compensate DC-link Voltage Ripple for Four-switch Three-phase Voltage-source Inverters, IEEE Transactions on Power Electronics, Vol. 14, No. 4, July 1999, pp.743 – 752.

[8] Modern Power Electronics and AC drives by Bose, Bimal K.

[9] POWER ELECTRONICS Converters, Applications and Design by Ned Mohan

[10] Speed Control of 3-Phase Induction Motor Using PIC18 Microcontrollers.

[11] M B de Rossiter Correa, Member , IEEE cursino Brandao jacobina Senior Member IEEE, Edison Roberto Cabral Da Silva, Fellow IEEE and Antonio Marcus Nogueria Lima, Member IEEE " A general PWM Statergy for four switch three phase inverter,IEEE TRANSACTIONS ON POWER ELECTRONICS, VOL. 21, NO. 6, NOVEMBER 2006

[12] Mrs. M Shanmugapriya P G Student, Mrs Prawin Angel Michel, Assistant Profrssor EEE, Ksrunya University Coimbatore," Sensorless control of an FSTPI using FPGA" IEEE international Conference on Advances in Science and management march 31-2012

Curve Veering in Rotor-Bearing Systems Using Finite Element Method

Mohammad Razi[#1], Ali Fellah Jahromi[#2], Rama B. Bhat[#3], Ashok Kaushal[#4] and Ayman Surial[#5]
[#]*Department of Mechanical and Industrial Engineering*
Concordia University, Montreal, QC, Canada
mo_razi@encs.concordia.ca[1], al_fel@encs.concordia.ca[2], rbhat@encs.concordia.ca[3],
ashok_kaushal@hotmail.com[4] and asurial@yahoo.ca[5]

***Abstract*— When natural frequencies of a vibrating system are plotted against a system parameter, sometimes two natural frequencies which appear to cross each other at some point, strangely veer away without crossing. The phenomenon is called "curve veering", and the mode shapes of the vibrating system change drastically in the vicinity of such veering. In rotating systems the characteristics such as critical speed are influenced by the rotational speed, and hence the rotational speed is a system parameter. Campbell diagrams which are plots of natural frequencies against the running speed of the rotor were observed to show the curve veering behavior. By suitable design changes in the rotor-bearing system it is possible to avoid such curve veering. The results showing the curve veering behavior and design changes which remove such curve veering are presented and discussed.**

Keywords—Curve Veering, Finite Element Method, Gyroscopic Effect, Campbell Diagram

I. INTRODUCTION

The phenomenon of "curve veering" is sometimes observed in vibrating systems when the natural frequencies or eigenvalues are plotted against a system parameter such as the aspect ratio, non-homogeneities, or material properties. The curve veering behavior could be due to the approximate nature of the analysis or it may be due to the inherent nature of the system itself [1, 2, 3, 4]. Leissa [1] described the curve veering as a phenomenon where "…. the [eigenfunctions] must undergo violent change - figuratively speaking, a dragonfly one instant, a butterfly the next, and something indescribable in between. Thus the results appear strange from an esthetic view point." Leissa used the Galerkin's method, which is an approximate method, to solve for the vibrations of a fixed rectangular membrane, where curve veering occurs in view of the numerical approximation involved [1]. Such seeming occurrences of curve veering can take place when vibrating systems are analyzed using approximate methods such as the Gelerkin's method or the Rayleigh Ritz method [3 –10]. Since discretization of continuous structures is an approximation, curve veering can occur in finite element analysis of the vibration of structures. More detailed examination in the vicinity of the apparent crossing points need to be carried out in order to determine whether they are truly crossing points or whether they involve curve veering.

If the phenomenon of "curve veering" is inherent nature of the vibrating system, the response quantities such as the deflection or the stresses, will be completely misleading in view of the sudden changes in the mode shapes in the vicinity, resulting in erroneous design. In such situations it is advisable to solve the problem using different methods and verify whether the curve veering is due to the approximate nature of the analysis or it is due to the inherent nature of the system.

In the present study, curve veering phenomenon is examined in a rotor-casing system. The rotor-casing system is discretized using finite element modeling.

The paper is organized in four sections. The first section provides an introduction to the phenomenon of curve veering in mechanical systems. The second section describes the methodology and modeling of the rotor system including the geometry, material properties, and the gyroscopic effect. The third section provides a brief description of the analysis and the fourth section presents the results which includes cases with and without curve veering. Finally, the conclusions of the study are presented.

II. METHODOLOGY AND MODELING

The simple Jeffcott rotor bearing system studied is shown in Fig. 1.

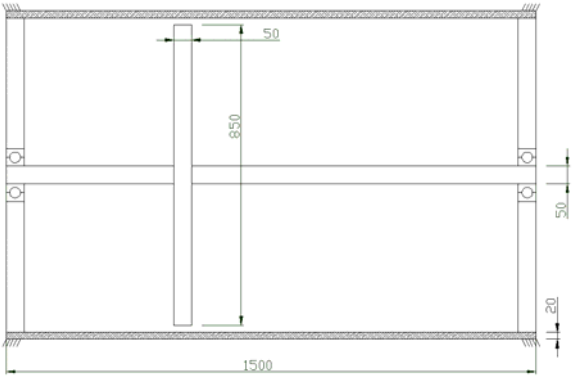

Fig. 1. 2D cross section of the rotor and casing geometry

A simple rotor-casing model consisting of a slender shaft of diameter 0.05 m and length 1.5 m, carrying a disk of diameter 0.85 m, and thickness 0.05 m, and a cylindrical casing with thickness 0.02 m and length equal to that of the rotor shaft is considered for the study. The disk is located at 1 meter from the right end of the shaft in order to magnify the gyroscopic effect in second bending frequency of the shaft which is close to a casing frequency. The material for both shaft and disk is considered as steel (linear and isotropic) with properties as given in Table I. The rotor model is shown in Fig. 2.

TABLE I. MATERIAL PROPERTIES

Modulus of Elasticity, N/m^2	***Poisson's Ratio***	***Density, kg/m^3***
$2x10^{11}$	0.3	7860

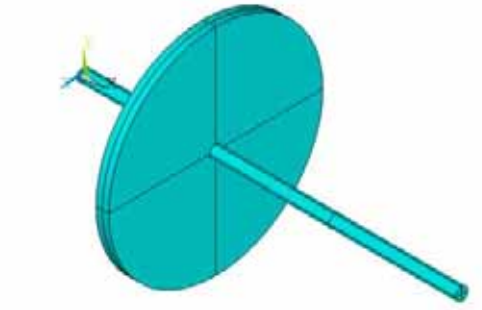

Fig. 1. Rotor model in ANSYS

The model is defined by key points in ANSYS on the planar cross section of the model above the shaft axis. This is revolved around the shaft axis in order to obtain the three dimensional axisymmetric structure. The SOLID187 element in ANSYS supports the gyroscopic effect and hence is used for the rotor dynamic analysis [11]. The model is meshed using 10-node, tetrahedral elements in ANSYS.

The connection between the rotor and the casing is modeled using COMBIN14 element representing the damping and spring effect of bearing [11], and the RBE3 element which distributes the loads from the master node located on the bearing to the slave nodes on the casing. The master node of the RBE3 element is located at a virtual node located on casing coincident with a point on the shaft axis. Thus the COMBIN14 element, which represents an isotropic bearing, has one of its nodes on the rotating shaft axis while the other end is connected to the master node of the RBE3 element which is on the casing.

Figure 3 shows the assembly of the rotor and casing considering RBE3 and COMBIN14 elements.

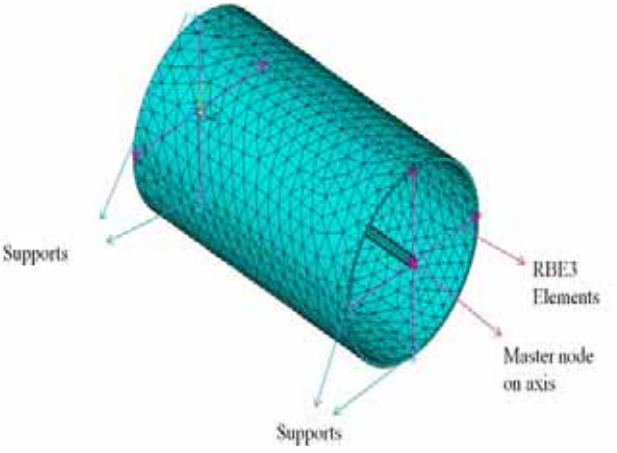

Fig. 2. Assembly mesh model of rotor, casing and bearing in ANSYS

The gyroscopic effect causes a split in the natural frequencies of the rotor, depending on its direction of rotation, when the running speed of the rotor is increased. The Coriolis Effect is activated for all the rotating elements in the analysis of ANSYS in order to account for the changing distance from the rotational axis resulting in a change of centrifugal loads. In addition, the modal analysis type is QR damped as required to include the Coriolis Effect.

In order to model the rotating shaft, disk and the stationary casing, the rotor should be modeled and meshed in the first step. In the next step the casing should be modeled and meshed separately. Then, The RBE3 and COMBIN14 elements are introduced in between the casing and rotor as explained earlier. Finally, the rotational speed command is applied only on the rotating part of the system through the appropriate option in ANSYS. In addition, the (prcamp) and (plcamp) options on the rotary part should be applied in order to plot the Campbell diagram.

I. ANALYSIS

The equations of motion of the system is obtained as

$$[M]\{\ddot{x}\}+[C+G(\omega)]\{\dot{x}\}+[K]\{x\}=\{f(t)\} \quad (1)$$

where [M], [C], and [K] are the mass, damping and stiffness matrices, respectively, [G(ω)] is the gyroscopic matrix, ω is the running speed of the rotor, and {f(t)} is the vector of external forces acting on the structure. The natural frequencies are obtained by solving the homogeneous form of Eq. (1). The natural frequencies are influenced by the gyroscopic terms and depend on the sense of rotation, ω. For positive rotational speeds the natural frequencies go on increasing with the speed and the rotor whirl is in the forward direction while for negative rotational speeds the direction of whirl is reversed resulting in backward whirl. When the speed of rotation is zero there is only one frequency corresponding to a particular mode whereas when the speed of rotation is finite the natural frequencies for those particular modes are split with the forward whirl frequency increasing and the backward whirl frequency decreasing.

When the natural frequencies coincide with the speed of rotation of the rotor, this constitutes a critical speed of the rotor.

II. Results And Discussion

The casing is fixed at two points at each end of the casing shell as shown in Fig. 3. The Campbell diagram for this case is shown in Fig.4. In obtaining the Campbell diagram, the natural frequencies are calculated with speed steps of 50 rad/sec. The speed dependent natural frequencies of the rotor due to the gyroscopic effects show the forward and the backward in Fig. 4. Curve veering phenomenon occurs between the second bending frequency of the shaft (involving the gyroscopic split in the frequencies) and first frequency of casing (which is speed independent) as shown in Fig. 4. The forward whirl curve appears to cross the speed independent frequencies at approximately 140 rad/sec and 225 rad/sec.

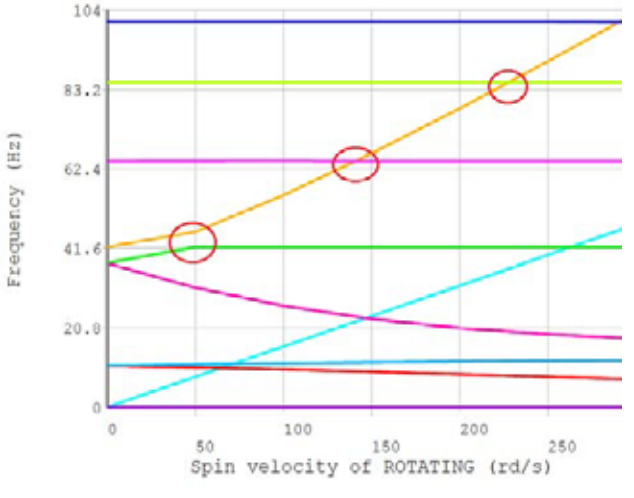

Fig. 3. Campbell Diagram for rotor with curve veering effect (case 1)

The results of ANSYS analysis for two bending frequencies of the shaft and casing frequencies at 7 different load steps are presented in Tables II and III. The casing frequencies are identified as those which are speed independent.

Tables II and III show that the forward frequency of second bending mode of rotor in 50 (rad/sec) is close to the first mode of the casing. The curve veering phenomenon is observed for the forward whirl frequency of the shaft veering away from the casing frequency.

In order to examine the curve veering at the first casing mode and the lack of curve veering at the second and third casing modes, the analysis was carried out with reduced speed steps of 1 rad/sec in the neighborhood of the apparent curve veering and curve crossing points.

TABLE II.
Rotor frequencies in Campbell diagram

	Natural frequencies						
No. of Modes	***0 rad/sec***	***50 rad/sec***	***100 rad/sec***	***150 rad/sec***	***200 rad/sec***	***250 rad/sec***	***300 rad/sec***
1	10.89	FW: 11.24 BW: 10.44	FW: 11.53 BW: 9.91	FW: 11.77 BW: 9.23	FW: 11.97 BW: 8.63	FW: 12.13 BW: 7.96	FW: 12.26 BW: 7.30
2	37.7	FW: 41.83 BW: 31.34	FW: 41.85 BW: 26.57	FW: 41.85 BW: 23.14	FW: 41.85 BW: 20.76	FW: 41.85 BW: 19.12	FW: 41.85 BW: 17.98

TABLE III.
Casing Natural frequencies

No. of Modes	***Natural frequencies***
2	41.895
3	64.472
4	85.064
5	100.91

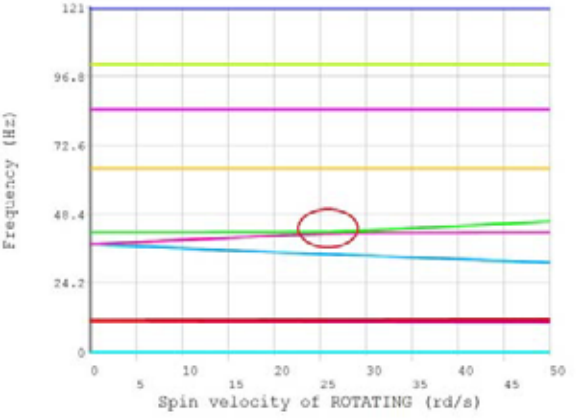

Fig. 5 Curve veering in the neighborhood of rotor speed of 25 rad/sec

The Campbell diagram in the neighborhood of 25 rad/sec is shown in Fig. 5. It can be seen that there is clear curve veering between the forward whirl frequency and the first casing mode.

The Campbell diagram in the neighborhood of 142.5 rad/sec is shown in Fig. 6. It can be seen that there is clear curve veering between the forward whirl frequency and the second casing mode.

The Campbell diagram in the neighborhood of 225 rad/sec is shown in Fig. 7. Again it can be seen that there is clear curve veering between the forward whirl frequency and the third casing mode.

It is clear from the Figs. 4, 5, 6, and 7 that the curve veering occurs between the speed dependent frequencies due to the gyroscopic effects and the speed independent frequencies which are the casing frequencies. In order to examine the effect of changing the casing mode frequencies on curve veering, the boundary conditions of the casing were changed by clamping more points on the casing. As a result the casing stiffness is increased shifting up the frequencies of the casing modes as shown in Figure 8. The first casing mode frequency has increased from 42 Hz to 85 Hz. As a result the forward whirl frequency does not meet the first casing frequency until much later. The curve veering is shifted from the speed of 25 rad/sec. From Fig. 8 it appears that there is no curve veering at the rotor speed of 230 rad/sec, however, if we minutely examine the neighborhood of these frequencies we can see that there is curve veering there also.

The curve veering effect will be of concern only when such veering takes place in the vicinity of the rotor critical speeds.

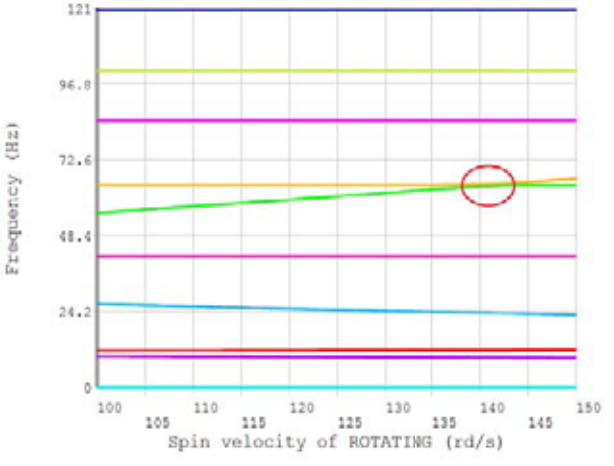

Fig. 6 Curve veering in the neighborhood of rotor speed of 142.5 rad/sec

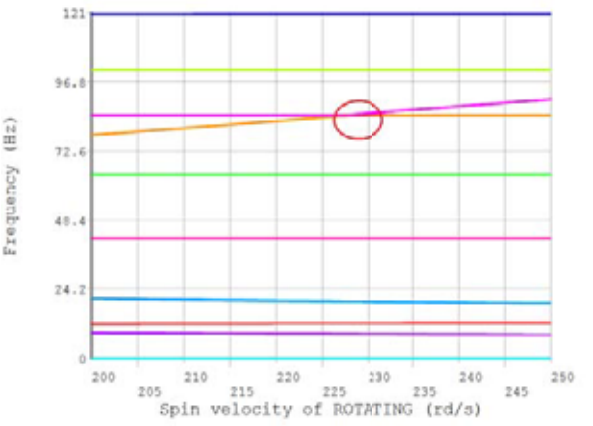

Fig. 7 Curve veering in the neighborhood of rotor speed of 225 rad/sec

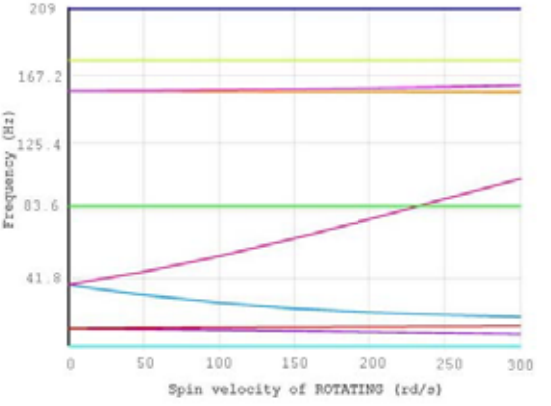

Fig. 8 Campbell Diagram with increased constraint on the casing

Table IV presents the numerical values for modal analysis of system for different angular velocities. Table IV and Fig. 8 present the trend of forward and backward frequencies of the rotor without effect of the curve veering.

TABLE IV.
ROTOR FREQUENCIES IN CAMPBELL DIAGRAM (CASE II)

	Natural frequencies						
No. of Modes	***0 rad/sec***	***50 rad/sec***	***100 rad/sec***	***150 rad/sec***	***200 rad/sec***	***250 rad/sec***	***300 rad/sec***
1	10.9	FW: 11.27 BW: 10.47	FW: 11.57 BW: 9.93	FW: 11.81 BW: 9.32	FW: 12.01 BW: 8.65	FW: 12.17 BW: 7.97	FW: 12.31 BW: 7.31
2	37.84	FW: 45.93 BW: 31.46	FW: 55.57 BW: 26.68	FW: 66.48 BW: 23.25	FW: 78.30 BW: 20.86	FW: 90.69 BW: 19.22	FW: 103.30 BW: 18.07
3	157.66	FW: 157.88 BW: 157.42	FW: 158.19 BW: 157.25	FW: 158.59 BW: 157.10	FW: 159.12 BW: 156.97	FW: 159.86 BW: 156.86	FW: 160.95 BW: 156.76

Table V presents the frequencies of the casing which are increased by increasing the number of boundary conditions of casing. This table shows that the first frequency of the casing is about twice the second natural frequency of the rotor in splitting point which avoids curve veering.

TABLE V.
CASING NATURAL FREQUENCIES (CASE II)

No. of Modes	***Natural Frequencies***
2	86.502
3	176.38
4	208.73

III. CONCLUSION

A methodology is developed for modeling a rotor system with casing considering the gyroscopic effect in ANSYS software. Based on the Campbell diagram plots, the curve veering phenomenon is presented. The results show that in numerical solution using Finite Element Method, the curve veering can occur if the constant frequencies of the system such as casing frequencies or axial mode of rotor which are not affected by angular velocity of the shaft occurs near the bending frequencies of the rotor. By changing the boundary conditions of the casing which has significant effect on constant frequencies of the casing it is possible to avoid the curve veering. The curve veering is of concern when it occurs near a critical speed of the rotor system.

ACKNOWLEDGMENT

The support from the NSERC-ENGAGE program is gratefully acknowledged.

REFERENCES

[1] W. Leissa, "On a curve veering aberration", *Journal of Applied Mathematics and Physics (ZAMP),* vol. 25, pp. 99-111, 1974.

[2] Kuttler, J.R. and V. G. Sigillito "On curve veering", Journal of Sound and Vibration, vol. 75, no. 4, p. 585, 1981.

[3] Perkins, N.C., and Mote C.D., JR, "Comments on curve veering in eigenvalue problems", *Journal of Sound and Vibration,* vol. 106, no. 3, p. 451, 1986.

[4] Bhat, R.B., "Curve veering: Inherent behaviour of some vibrating systems", *Shock and Vibration,* vol. 7, no. 4 p. 241, 2000.

[5] du Bois, J.L., "Eigenvalue curve veering in stressed structures: an experimental study", *Journal of Sound and Vibration*, vol. 322, no. 4, p. 1117, 2009.

[6] Liu, X.L., "Behavior of derivatives of eigenvalues and eigenvectors in curve veering and mode localization and their relation to close eigenvalues", *Journal of Sound and Vibration,* vol. 256, no. 3, p. 551, 2002.

[7] Balmes, E., "High modal density, curve veering, localization: a different perspective on the structural response", *Journal of Sound and Vibration,* vol. 161, no. 2, p. 358, 1993.

[8] Y.G. Jei and Y.J. Kim, "Modal Testing Theory of Rotor-Bearing Systems", *Journal of Vibration and acoustics, Transactions of ASME,* vol. 115, pp. 165–176, 1993.

[9] Y.G. Jei and C.-W. Lee, "Does curve veering occur in the eigenvalue problem of rotors?", *Journal of Vibration and acoustics, Transactions of ASME,* vol. 114, pp. 32–36, 1992.

[10] P.T. Chen and J.H. Ginsberg, "On the relationship between veering of eigenvalue loci and parameter sensitivity of eigenfunctions", *Journal of Vibration and Acoustics, Transactions of ASME,* vol. 114, pp. 141–148, 1992.

[11] ANSYS Inc., *Rotordynamic Analysis Guide.* Release 12.0, April 2009.

Effect of cutting parameters on cutting force and the surface roughness of Aluminium components using face milling process - A Taguchi Approach

Anil Antony Sequeira[#1], Ravikantha Prabhu[#2], N.S Sriram [*3], Thirumaleshwar Bhat#4
[#]*Department of Mechanical Engineering,*
St. Joseph Engineering College, Mangalore - 575 028 Karnataka INDIA.
[1]sequeiraanil@yahoo.com
**Department of Mechanical Engineering, Vidya Vikas Institute of Engineering and Technology,*
Mysore, Karnataka State, 570028.
[3]nittesriram@yahoo.com

***Abstract*—Aluminum is used excessively in the modern world, and the uses of the metal are extremely diverse due to its many unusual combinations of mechanical and chemical properties. They have been widely used in industries, especially aerospace industries. However, machining of Aluminium involves expensive tooling cost at the expense of getting good surface finish. The study investigated the optimum parameters that could produce significant good surface finish and optimum cutting force whereby reducing tooling cost. It employed the Taguchi design method to optimize the surface roughness quality and cutting force in a Computer Numerical Control (CNC). The milling parameters evaluated are cutting speed, feed rate and depth of cut. An $L_9(3^4)$ orthogonal array, signal-to-noise (S/N) ratio and analysis of variance (ANOVA) are employed to analyze the effect of these cutting parameters. The analysis of the result indicated that the optimal combination for low resultant cutting force and good surface finish are high cutting speed, low feed rate and low depth of cut. The study shows that the Taguchi method is suitable to solve the stated problem with minimum number of trials as compared with a full factorial design.**

I. INTRODUCTION

Robust design is an engineering methodology for obtaining product and process conditions, which are minimally sensitive to the various causes of variation to produce high-quality products with low development and manufacturing costs [1]. Taguchi's parameter design is an important tool for robust design. It offers a simple and systematic approach to optimize design for performance, quality and cost. Two major tools used in robust design are [1–6]:

- Signal to noise ratio, which measures quality with emphasis on variation, and
- Orthogonal arrays, which accommodate many design factors simultaneously.

When a critical quality characteristic deviates from the target value, it causes a loss [2]. Continuously pursuing variability reduction from the target value in critical quality characteristics is the key to achieve high quality and reduce cost.

The successful applications of Taguchi methods by both engineers and statisticians within British industry have lead to the formation of UK Taguchi Club [4]. Taguchi's approach is totally based on statistical design of experiments [1], and this can economically satisfy the needs of problem solving and product/process design optimization [5]. By applying this technique one can significantly reduce the time required for experimental investigation, as it is effective in investigating the effects of multiple factors on performance as well as to study the influence of individual factors to determine which factor has more influence, which less [1,6]. Some of the previous works that used the Taguchi method as tool for design of experiment in various areas including metal cutting are listed in Refs. [7–10]. This paper describes a case study on face milling parameters at three levels each. The main objective is to find a combination of milling parameters to achieve low cutting force and surface roughness.

Numerous roughness height parameters such as average roughness, smoothening depth, root mean square and maximum peak-to-valley height can be closely correlated. This study uses average roughness for the characterization of surface roughness, due to the fact that it is widely adopted in the industry for specifying the surface roughness. Mital and Mehta [13] have conducted a survey of the previously developed surface roughness prediction models and factors influencing the surface roughness. They have found that most of the surface roughness prediction models have been developed for steels.

II. MATERIAL AND METHODS

A. *Material*

Aluminum is a soft, lightweight, malleable metal with appearance of a silver-white metal obtained from bauxite. The appearance may range from silvery to dull gray, depending on the surface roughness. The yield strength of pure Aluminum is 7–11 MPa, while Aluminum alloys have yield strengths ranging from 200 MPa to 600 MPa.

Aluminum has about one-third the density and stiffness of steel. It is ductile, and easily machined, cast, and extruded. Aluminum is a good thermal and electrical conductor, by weight better than copper. Aluminum is capable of being a superconductor, with a superconducting critical temperature of 1.2 Kelvin and a critical magnetic field of about 100 gauss.

B. *Taguchi method*

The Taguchi method, which is effective to deal with responses, was influenced by multi-variables. This method drastically reduces the number of experiments that are required to model the response function compared with the full factorial design of experiments. The Taguchi technique is devised for process optimization and identification of optimal combination of the factors for a given response. This technique is divided into three main phases, which encompasses all experimentation approaches. The three phases are (1) the planning phase (2) the conducting phase and (3) the analysis phase. Planning phase is the most important phase of the experiment. This technique creates a standard orthogonal array to accommodate the effect of several factors on the target value and defines the plan of experiments. The experimental results are analyzed using analysis of means and variance to study the influence of factors.

C. *Design of experiment*

Design of experiment is the powerful analysis tool for modeling and analyzing the influence of the control factors on the performance output. The most important stage in the design of experiment lies in the selection of the control factors. The operating conditions, under which measurement of cutting force is carried out, are given in Table I under room temperature.

Three parameter, viz., Feed Rate, Spindle Speed and Depth of Cut each at three levels, are considered in this study in accordance with $L_9(3^4)$ orthogonal array design. The plan of the experiment is as follows: the first column is assigned to the Feed Rate (A), the second column to the Spindle speed (B), the fourth column to the Depth of Cut (C).

TABLE I

CONTROL FACTORS AND THEIR LEVELS

Parameters	Level 1	Level 2	Level
Feed Rate(mm/min)	400	800	1600
Spindle Speed(rpm)	1300	1800	2600
Depth of cut(mm)	0.7	1.2	1.7

The experimental observations are transformed into signal-to-noise (S/N) ratio. There are several S/N ratios available depending on the type of characteristic, which can be calculated as logarithmic transformation of the loss function by the following equation:

Lower is the better characteristic,

$$\frac{S}{N} = -10\log\frac{1}{n}(\sum y^2) \quad (1)$$

Where 'n' is the number of observations, and 'y' the observed data. "Lower is the better" (LB) characteristic, with the above S/N ratio transformation, is suitable for minimization of cutting force and coefficient of friction.

D. *Surface roughness evaluation*

There are various simple surface roughness amplitude parameters used in industry, such as roughness average (R_a), root-meansquare (rms) roughness (R_q), and maximum peak-to-valley roughness (R_y or R_{max}), etc (Joseph and John, 2001). Since Ra and R_q are the most widely used surface parameters in industry, Ra was selected to express the surface roughness in this study. Figure 1 shows the average roughness (R_a) is the area between the roughness profile and its mean line, or the integral of the absolute value of the roughness profile height over the evaluation length. The R_a is specified by the following equation:

$$Ra = \frac{1}{L}\int_0^L |Y(x)|\, dx \ (\mu m) \quad (2)$$

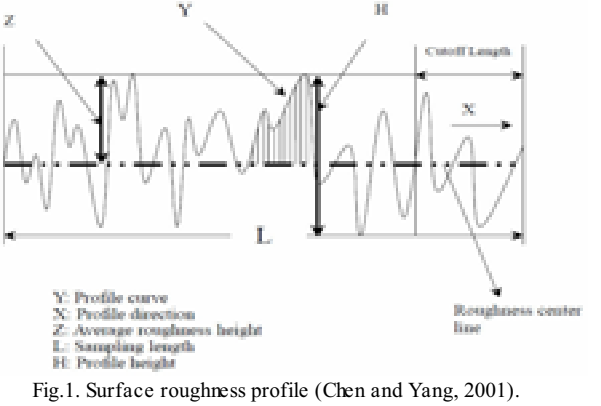

Fig.1. Surface roughness profile (Chen and Yang, 2001).

E. Machining parameter

To improve the quality of surface roughness of Aluminium alloys and processes with minimum cost and time constraints, the Taguchi parameter design techniques are applied in design of experiment (DOE). Minimum surface roughness average (R_a) was carried out since the value represents better or improved surface roughness. Therefore, a smaller-the-better method is implemented in this experiment (Mori, (1990)). The controllable parameters are selected because of their potential effects on surface roughness performance in face milling operations. The parameters are the cutting speed denoted as (A), the feed rate denoted as (B), the depth of cut denoted as (C). By applying cutting speed, feed rate, depth of cut and type of milling cutter as control factors and used them to measure responses for surface roughness, signal-to-noise ratio can be calculated to determine the optimum cutting condition (Lou MS et al., (1998)).

F. Experimental Setup

The machining of the specimen is performed using a BFW Agni BMV 45 T20 CNC vertical axis milling machine. The milling cutter used for experimentation is SECO R220.69-12 grade. The tool holder used for experimentation was BT 40 grade. Face Milled components are shown in Figure 2. A Mitutoyo Surf test SJ-301 profilometer was used to measure surface roughness (R_a) of the machined components. Variation in the cutting force during the machining is calculated indirectly using the spindle power. The average cutting force measured along x y and z axes called the F_x,F_y and F_z respectively.

Fig.2. Face milled Aluminium workpieces.

III. RESULTS AND DISCUSSIONS

I. Analysis of Experimental Results

The experimental data for cutting force and roughness is reported in the Table II. From Table II, the overall mean for the S/N ratio of the cutting force Fx, Fy, Fz and the roughness are found to be -54.32db, - 51.59 db and 8.34 db respectively. The analyses of the experimental data are carried using the software MINITAB 15 specially used for design of experiment applications.

II. Analysis of S/N

Figs. 3-5 showed the main effects plot for S/N ratios. The level of a factor with the highest S/N ratio was the optimum level for responses measured.

From the S/N ratio analysis in Figs. 1-3, the optimal machining conditions were 400 mm/min feed rate (level 1), 2600 rpm spindle speed (level 3) and 0.7 mm depth of cut (level 1) for cutting speed F_x, F_y and F_z.

TABLE II EXPERIMENTAL RESULTS

Feed Rate (A)	Spindle Speed (B)	Depth of Cut (C)	F_X	S/N Ratio	F_Y	S/N Ratio	F_Z	S/N Ratio	R_a	S/N Ratio
400	1300	0.7	392	-51.8657	235.2	-47.4287	490	-53.8039	0.18	14.8945
400	1800	1.2	588	-55.3875	274.4	-48.7677	490	-53.8039	0.11	19.1721
400	2600	1.7	392	-51.8657	235.2	-47.4287	490	-53.8039	0.39	8.1787
800	1300	1.7	862.4	-58.7142	784	-57.8863	637	-56.0828	0.48	6.3752
800	1800	0.7	392	-51.8657	274.4	-48.7677	490	-53.8039	0.23	12.7654
800	2600	1.2	705.6	-56.9712	274.4	-48.7677	588	-55.3875	0.3	10.4576
1600	1300	1.2	823.2	-58.3101	784	-57.8863	637	-56.0828	0.55	5.1927
1600	1800	1.7	705.6	-56.9712	509.6	-54.1446	686	-56.7265	0.31	10.1728
1600	2600	0.7	392	-51.8657	235.2	-47.4287	539	-54.6318	0.44	7.1309

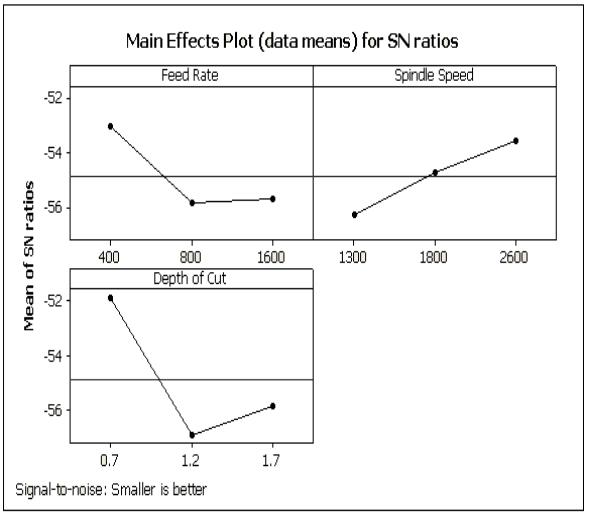

Fig.3. S/N ratio values for F_x

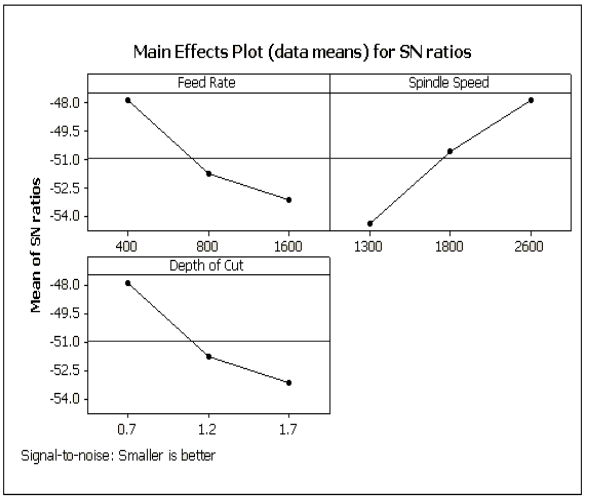

Fig.4. S/N ratio values for F_y

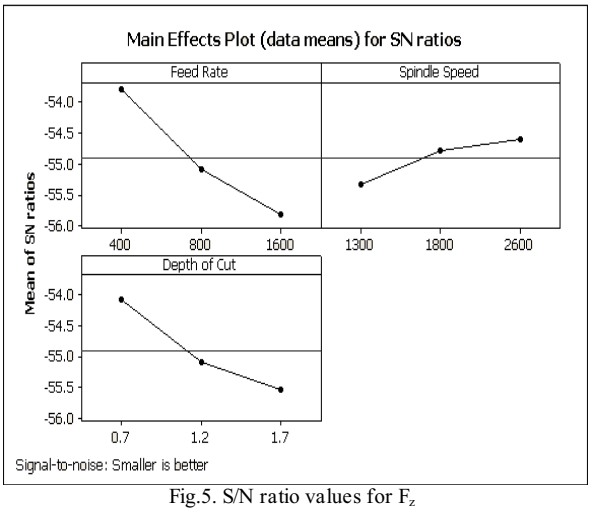

Fig.5. S/N ratio values for F_z

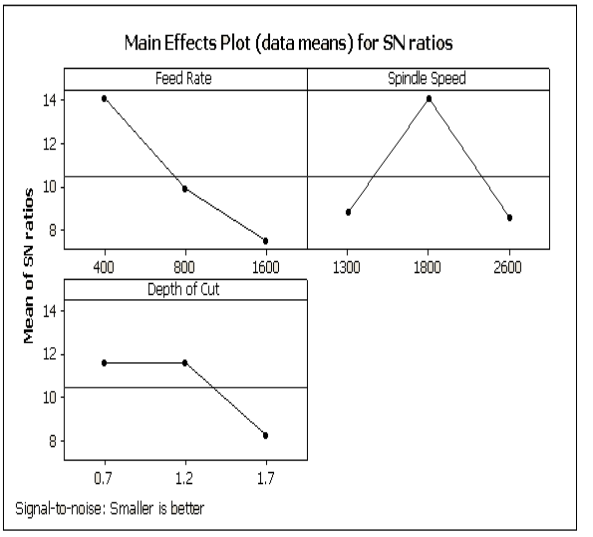

Fig.6. S/N ratio values Surface Roughness

From Fig .6 the optimal machining conditions were 400 m/min feed rate (level 1), 1800 rpm spindle speed (level 2) and 0.7 mm depth of cut (level 1) for surface roughness respectively.

III. Analysis of Variance (ANOVA)

ANOVA was used to determine the significant parameters influencing the force components and surface roughness in the milling of Aluminium specimen. Tables III, IV, V and VI showed the summary of S/N values and ANOVA results for cutting force F_x, F_y, F_z and surface roughness, respectively. In this study, analysis was a level of significance as 5% and level of confidence as 95%.

In order to understand a concrete visualization of impact of various factors effect on the output performance, it is desirable to develop analysis of variance (ANOVA) table to find out the order of significant factors. From Table III one can observe that the depth of cut (p=0.072) has greater static influence of 58.76% followed by feed rate (p=0.179) has an influence of 20.99% and spindle speed (p=0.226) has an influence of 15.65% on cutting force F_x.

From Table IV one can observe that the spindle speed (p=0.046) has greater static influence of 40.87% followed by feed rate and depth of cut (p=0.0.064) has an influence of 28.58% on cutting force F_y.

From Table V one can observe that the feed rate (p=0.120) has greater static influence of 55.27% followed by depth of cut (p=0.202) has an influence of 29.76% and spindle speed (p=0.502) has an influence of 7.45% on cutting force F_z.

TABLE III
SUMMARY OF S/N VALUES AND ANOVA RESULTS FOR FX

Factors	Degrees of Freedom DF	Average S/N Values			Sum of Square	Mean Square	F	P	Percentage of Contribution (%)
		Level 1	Level 2	Level 3					
Feed Rate	2	-53.04	-55.85	-55.72	15.079	7.540	4.58	0.179	20.99
Spindle Speed	2	-56.30	-54.74	-53.57	11.245	5.622	3.42	0.226	15.65
Depth of Cut	2	-51.87	-56.89	-55.85	42.197	21.098	12.82	0.072	58.76
Error	2				3.292	1.646			4.60
Total	8				71.812				100

S = 1.28289 R-Sq = 95.42% R-Sq (adj) = 81.67%

TABLE IV
SUMMARY OF S/N VALUES AND ANOVA RESULTS FOR FY

Factors	Degrees of Freedom DF	Average S/N Values			Sum of Square	Mean Square	F	P	Percentage of Contribution (%)
		Level 1	Level 2	Level 3					
Feed Rate	2	-47.88	-51.81	-53.15	45.133	22.566	14.51	0.064	28.58
Spindle Speed	2	-54.40	-50.56	-47.88	64.539	32.270	20.74	0.046	40.87
Depth of Cut	2	-47.88	-51.81	-53.15	45.133	22.566	14.51	0.064	28.58
Error	2				3.111	1.556			1.97
Total	8				157.916				100

S = 1.24724 R-Sq = 98.03% R-Sq(adj) = 92.12%

TABLE V
SUMMARY OF S/N VALUES AND ANOVA RESULTS FOR FZ

Factors	Degrees of Freedom DF	Average S/N Values			Sum of Square	Mean Square	F	P	Percentage of Contribution (%)
		Level 1	Level 2	Level 3					
Feed Rate	2	-53.80	-55.09	-55.81	6.2185	3.1092	7.36	0.120	55.27
Spindle Speed	2	-55.32	-54.78	-54.61	0.8379	0.4190	0.99	0.502	7.45
Depth of Cut	2	-54.08	-55.09	-55.54	3.3478	1.6739	3.96	0.202	29.76
Error	2				0.8450	0.4225			7.52
Total	8				11.2491				100

S = 0.649991 R-Sq = 92.49% R-Sq (adj) = 69.95%

From Table VI one can observe that the feed rate (p=0.188) has greater static influence of 41.26% followed by spindle speed (p=0.213) has an influence of 35.21% and depth of cut (p=0.406) has an influence of 13.96% on surface roughness.

TABLE VI
SUMMARY OF S/N VALUES AND ANOVA RESULTS FOR ROUGHNESS

Factors	Degrees of Freedom DF	Average S/N Values			Sum of Square	Mean Square	F	P	Percentage of Contribution (%)
		Level 1	Level 2	Level 3					
Feed Rate	2	14.082	9.866	7.499	66.712	33.356	4.32	0.188	41.26
Spindle Speed	2	8.821	14.037	8.589	56.937	28.469	3.69	0.213	35.21
Depth of Cut	2	11.597	11.607	8.242	22.580	11.290	1.46	0.406	13.96
Error	2				15.447	7.724			9.57
Total	8				161.677				100

S = 2.77916 R-Sq = 90.45% R-Sq (adj) = 61.78%

IV. CONCLUSION

This study discussed an application of Taguchi experimental method for investigating the influence of milling parameters on cutting force and surface roughness during milling of Aluminum. In the milling experiments, different cutting speed, feed rate and depth of cut were utilized. The level of importance of the machining parameters on the cutting force and surface roughness was determined by ANOVA. Based on this study, the following conclusions can be drawn for the milling conditions:

1. The optimal machining conditions were 400 mm/min feed rate (level 1), 2600 rpm spindle speed (level 3) and 0.7 mm depth of cut (level 1) for cutting speed F_x, F_y and F_z.
2. The optimal machining conditions were 400 m/min feed rate (level 1), 1800 rpm spindle speed (level 2) and 0.7 mm depth of cut (level 1) for surface roughness.
3. The depth of cut had a greater static influence followed by feed rate and spindle speed on cutting force component F_x.
4. The spindle speed had greater static influence followed by feed rate and depth of cut on cutting force component F_y.
5. The feed rate has greater static influence followed by depth of cut and spindle speed on cutting force component F_z.
6. The feed rate has greater static influence followed by spindle speed and depth of on surface roughness.

V. REFERENCES

[1] S.H. Park, Robust Design and Analysis for Quality Engineering, Chapman & Hall, London, 1996.

[2] J.A.Ghani, I.A. Choudhury, H.H. Hassan, "Application of Taguchi method in the optimization of end milling parameter", Journal of Materials Processing Technology, Vol.145, 2004, pp. 84–92.

[3] J. Kopac , P. Krajnik, "Robust design of flank milling parameters based on grey-Taguchi method", Journal of Materials Processing Technology, Vol.191, 2007, pp. 400–403.

[4] T. Bendell, Taguchi methods, in: Proceedings of the 1988 European Conference on Taguchi Method, Elsevier, Amsterdam, 13–14 July, 1988.

[5] Julie Z. Zhang, Joseph C. Chen, E. Daniel Kirby, "Surface roughness optimization in an end-milling operation using the Taguchi design method", Journal of Materials Processing Technology, Vol.184, 2007, pp. 233–239.

[6] E. Kuram, B. T. Simsek, B. Ozcelik, E. Demirbas, and S. Askin "Optimization of the

Cutting Fluids and Parameters Using Taguchi and ANOVA in Milling" World Congress on Engineering, Vol II, 2010, pp. 978-988.

[7] W.H. Yang, Y.S. Tarng, Design optimisation of cutting parameters forturning operations based on the Taguchi method, J. Mater. Process. Technol. 84 (1998) 122–129.

[8] T.R. Lin, Experimental design and performance analysis of tin-coated carbide tool in face milling stainless steel, J. Mater. Process. Technol. 5654 (2002) 1–7.

[9] K.L. Tsui, Modeling and analysis of dynamic robust design experiments, IEE Trans. 31 (1999) 113–1122.

[10] Zhang, H.P. Wang, Robust design of assembly and machining tolerance allocations, IEE Trans. 30 (1998) 17–29.

[11] Lou MS, Chen JC, Li MC, "Surface Roughness Prediction Technique for CNC End-Milling", J. Ind. Technology Vol.15, No.1, 1998, pp.1-6.

[12] Chen JC, Yang JL (2001), A Systematic Approach for Identifying Optimum Surface Roughness Performance in End-Milling Operations. J. Ind. Technol., 17 (2): 1-8.

[13] Mital, M. M., 1988. "Surface roughness prediction models for fine turning", Int. J. Prod. Res.26, pp. 1861–1876.

[14] Mori T (1990), The New Experimental Design: Taguchi's Approach to Quality Engineering, ASI Press, Dearborn

[15] Lou MS, Chen JC, Li MC (1998). "Surface Roughness Prediction Technique For CNC End-Milling", J. Ind. Technol., 15(1): 1-10.

Abrasive Wear Performance of Epoxy/Glass/PTW Composites

Sudheer M[#1], SandeshKubanooraya[#2], Raju K[#3], Thirumaleshwara Bhat[#4]
[#]*Department of Mechanical Engineering, St. Joseph Engineering College, Mangalore Karnataka-575028, India*
[1]Research Scholar:msudheerm2002@yahoo.co.in[corresponding author]
[2]PG Student:sandesh.udupi@gmail.com
[3]Professor:rajuksjec@rediffmail.com
[4]Professor and Head:tbhatsjec@gmail.com

***Abstract*— Thispaper discusses two-body abrasive wear behaviour of Potassium Titanate Whisker (PTW) reinforced vacuum moulded epoxy/glass composites. The effects of whisker content, sliding distance, normal load and abrasive grit size on wear behaviour of composites were evaluated by pin-on-paper abrasion tests. The tests were conducted at ambient conditions and constant disc speed of 200 rpm. The wear loss of composites was found increasing with the increase in normal loads, abrading distances and coarser abrasive papers. The effect of whisker content to minimize wear loss was highly dependent on abrasive grit sizes. The friction coefficient has shown decreasing trend with normal load and mixed trend with sliding distance and whisker content.The scanning electron microscope (SEM) images of composite specimen worn at higher loads, distances and for finer abrasive grit sizes were evaluated and results indicate more severe damage to epoxy/glass composites as compared to PTW filled epoxy/glass composites.**

***Keywords*— Two body abrasion, ceramic whiskers, glass fibers, polymer composites, wear mechanisms**

I. Introduction

Wear is defined as damage to a solid surface, generally involving progressive loss of material, due to relative motion between contacting surfaces. The five main types of wear are abrasive, adhesive, fretting, erosion and fatigue wear, which are commonly observed in practical situations. Abrasive wear is the most important among all the forms of wear because it contributes almost 63% of the total cost of wear [1]. Nowadays Polymer Matrix Composites (PMCs) are increasingly employed in various industrial equipments that are subjected to abrasive wear situations. This includes highly abrasive wear systems such as conveyor aids, vanes and gears for pumps handling industrial fluids, sewage and abrasive contaminated water; bushes, seals and chute liners in agricultural, mining and earth moving equipment; roll-neck bearings in steel mill subjected to heat, shock loading, water; and guides in bottle handling plants [2].

A literature survey indicated that fiber reinforcement along with ceramic fillers improved abrasive wear performance of polymers[3-8]. PTW is known to be an advanced multi-component ceramic whisker and its potential to reinforce with polymers and metals is currently being investigated by many researchers [9]. The studies done on PTW modified and fiber reinforced polymer composites are scanty as on date.

Hence, present work deals with preparation of epoxy/glass composites with varying percentage of PTW ceramic fillers and its characterization for abrasive wear performance.

II. Materials And Methods

A. Materials

Ambient temperature curing Epoxy resin (LY556) and triethylenetetramine (TETA)hardener (HY951) supplied by M/s. Huntsman advanced materials India Pvt. Ltd., Bengaluru, India was used as matrix material. The plain weave E-glass fibers of aerial density 212 g/m^2, obtained from M/s. Arun fabrics, Bngaluru, India were used as main reinforcement. The PTW fillers used as secondary reinforcement were supplied by Hangzhou Dayangchem Co. Ltd., Hong Kong, China. These fillers are of whisker shape with diameters 0.5-2.5µm and lengths 10-100µm. The photo micrographs of glass fibers and PTW fillers are presented in Figs 1 and 2 respectively.

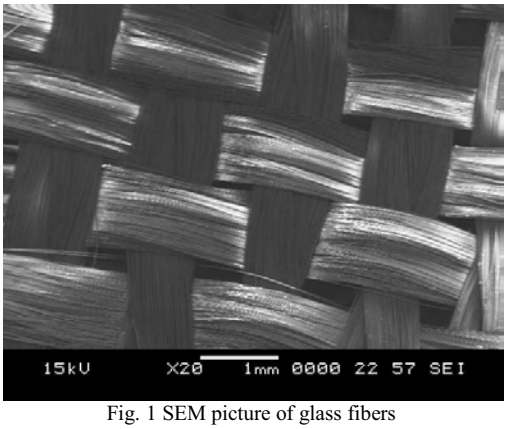

Fig. 1 SEM picture of glass fibers

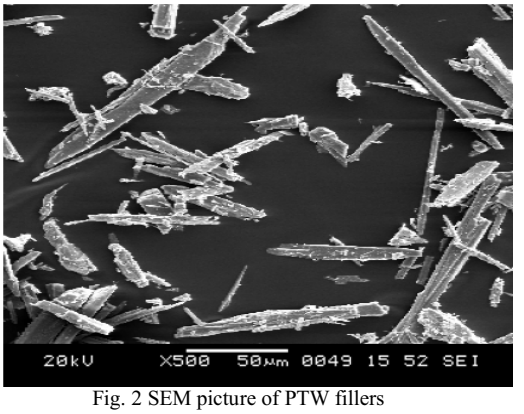

Fig. 2 SEM picture of PTW fillers

B. Composite Fabrication

The composites were prepared using vacuum bag molding technique. Epoxy/glass/PTW composites were prepared by varying the percentage (2.5, 5 and 7.5 wt%) of PTW fillers. Epoxy/glass composite without the fillers was also prepared for comparison purpose. The Fig 3 illustrates vacuum bag method. The detailed procedure can be referred elsewhere [10]. The composites prepared are designated as EG0, EG2.5, EG5 and EG7.5, numbers indicate weight percentage of PTW filler in composites.

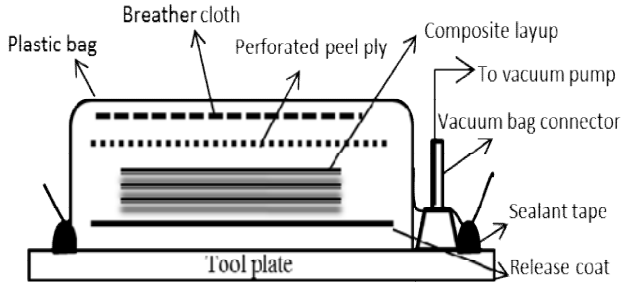

Fig. 3Vacuum bagging technique

C. Abrasive Wear Testing

Two-body abrasive wear tests were performed using a pin-on-disc machine (Model TR201C, DUCOM, Bengaluru, India) under multi-pass conditions. The composite specimen of 10×10×3 mm^3 with the rubbing surface of 10×10 mm^2 was glued to steel specimen of 10×10×30 mm^3 and rubbed against different abrasive papers. The abrasive paper was pasted on disc by means of suitable adhesive. The test configuration is illustrated in Fig 4. Before starting the experiment, composite surface was abraded against a fine abrasive paper of grade 800 to ensure uniform contact. The effects of various loads (5, 10 and 15 N), sliding distances (20, 40, 60 and 80 m) and abrasive papers (120, 320 and 600 grit size) under a constant sliding velocity (0.6283 m/s corresponding to 200 rpm) were studied. The wear in terms of weight loss was determined after each experiment using 0.1 mg digital weighing scale (Shimadzu AY220, Japan).Coefficient of friction (COF) is determined as ratio of frictional force measured from test machine to applied normal load. Each test conditions were repeated three times and average of the closest data was reported.

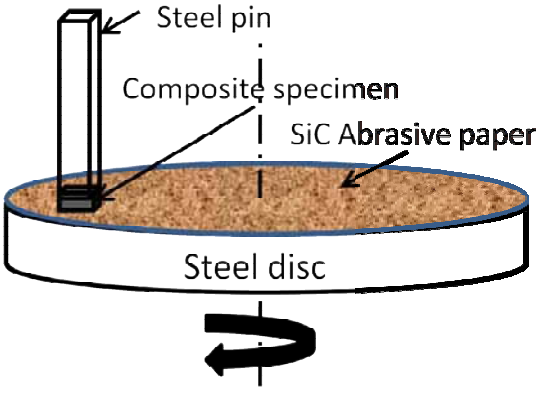

Fig. 4 Schematic of pin-on-disc configuration

III. Results And Discussion

A. Coefficient of Friction (COF)

Values of COF for different composites under varying loads and distances in case of 600 grit SiC paper are indicated in Table 1. COF values were found to decrease with applied load. This behaviour is in accordance with reports available in literatures [11]. However, with sliding distance, COF was found to initially increase and later decrease. During sliding, initially effective area at sliding interface steadily increases. This offers more frictional resistance. Hence COF tends to increase. However, with further sliding, clogging [4] in abrasive paper provides easy shear and tend to reduce COF values. The variation in COF with respect to filler content has shown no common trend. It is well known that friction and wear under abrasive mode is a more complex phenomenon. The transition between two-body and three-body contact [12] with testing parameters and several mechanisms simultaneously acting at sliding interface results in such varying trend of COF. Considering effect of abrasive grit size, COF values lied in range of 0.75-0.51 for 600 grade SiC paper, 0.87-0.48 in case of 320 gradeSiC paper and 0.84-0.32 in case of 120 grade SiC paper. Hence it is clear that range of COF values have narrowed down with finer abrasive papers. Thus almost stable COF is observed under mild abrasive wear sliding conditions.

B. Abrasive Wear Loss (AWR)

The effect of sliding distance on abrasive wear behaviour of composites for different abrasive papers is presented in the Fig 5. It can be observed that wear loss increases with sliding distance and it reduces with

finer abrasive papers. This is an expected behaviour in all types of composites. With increase in sliding distance, more material is removed from the composite surface and it results in increased wear loss. A close examination of Fig 5 indicates that wear loss increases at a higher rate during initial sliding (up to 40m distance) and later increases, but at a slower rate. This observation under multi-pass conditions is mainly because ofSiC particles loosing their abrasiveness with continuous sliding [5]. The wear loss was found to be dependent on counterface. In case of finer abrasive paper, small abrasive particles cause less damage to composite surface than coarser paper with large abrasive particles. Hence lesser wear loss was observed with finer abrasive papers.

The effect of normal load on abrasive wear behaviour of composites for different abrasive papers is presented in Fig.6. The wear performance observed is similar to that obtained for sliding distance effect. With increase in load, abrasives penetrate deeper into composite surface and increase material loss.

The effect of abrasive grit size on the wear behaviour can be interpreted from Fig. 7. It can be observed that, PTW has improved abrasive wear performance of epoxy/glass composites. However, optimum percentage of filler to minimize the wear loss was dependent on abrasive media. In case of 120 SiCpaper, EG2.5 composites performed best, where as EG5 composites showed minimum wear loss in case of 320 SiC paper.

TABLE 1.
COF VALUES FOR DIFFERENT SPECIMENS UNDER VARYING LOADS AND DISTANCES

		Sliding distance							
	Load	**10m**	**20m**	**30m**	**40m**	**50m**	**60m**	**70m**	**80m**
EG0	**5N**	0.670	0.720	0.680	0.700	0.690	0.640	0.620	0.610
	10N	0.645	0.700	0.710	0.680	0.690	0.675	0.660	0.645
	15N	0.550	0.560	0.576	0.545	0.535	0.530	0.535	0.525
EG2.5	**5N**	0.720	0.735	0.745	0.740	0.730	0.725	0.720	0.710
	10N	0.630	0.645	0.650	0.645	0.640	0.635	0.630	0.625
	15N	0.576	0.590	0.600	0.610	0.595	0.590	0.580	0.570
EG5	**5N**	0.740	0.750	0.735	0.720	0.730	0.725	0.715	0.710
	10N	0.660	0.680	0.675	0.660	0.665	0.655	0.645	0.640
	15N	0.596	0.610	0.625	0.615	0.600	0.590	0.580	0.560
EG7.5	**5N**	0.690	0.710	0.720	0.705	0.695	0.680	0.670	0.665
	10N	0.610	0.620	0.635	0.640	0.630	0.620	0.610	0.620
	15N	0.536	0.540	0.546	0.530	0.540	0.520	0.510	0.510

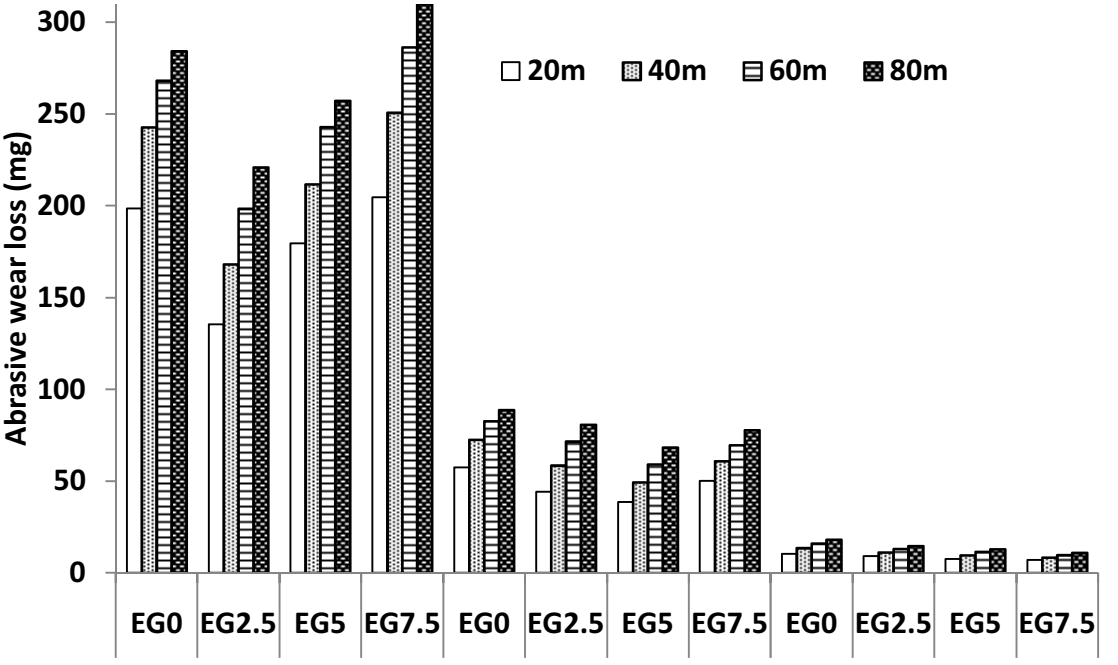

Fig. 5 Effect of sliding distance on abrasive wear loss of composites

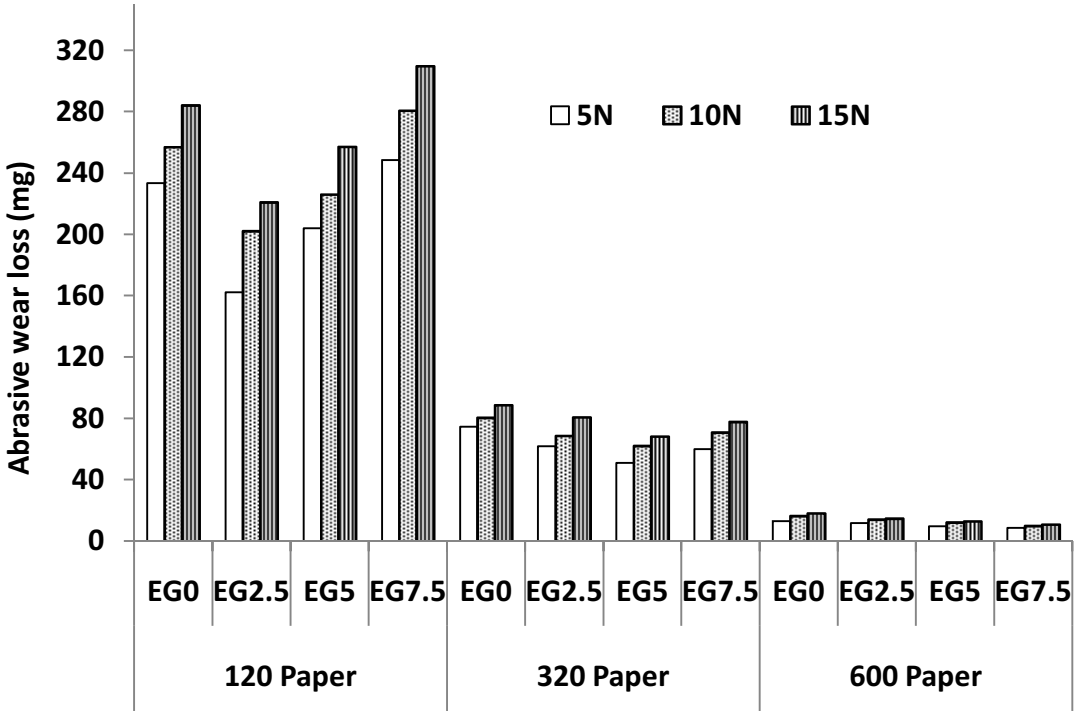

Fig.6 Effect of normal load on abrasive wear loss of composites

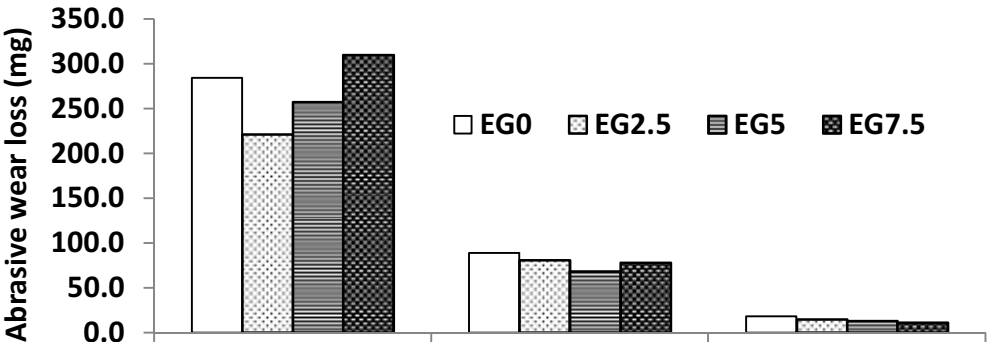

	120 paper	320 Paper	600 Paper
EG0	284.3	88.7	18.1
EG2.5	221.0	80.8	14.7
EG5	257.3	68.3	12.9
EG7.5	309.9	77.8	10.9

Fig. 7 Effect of abrasive grit size on abrasive wear loss of composites

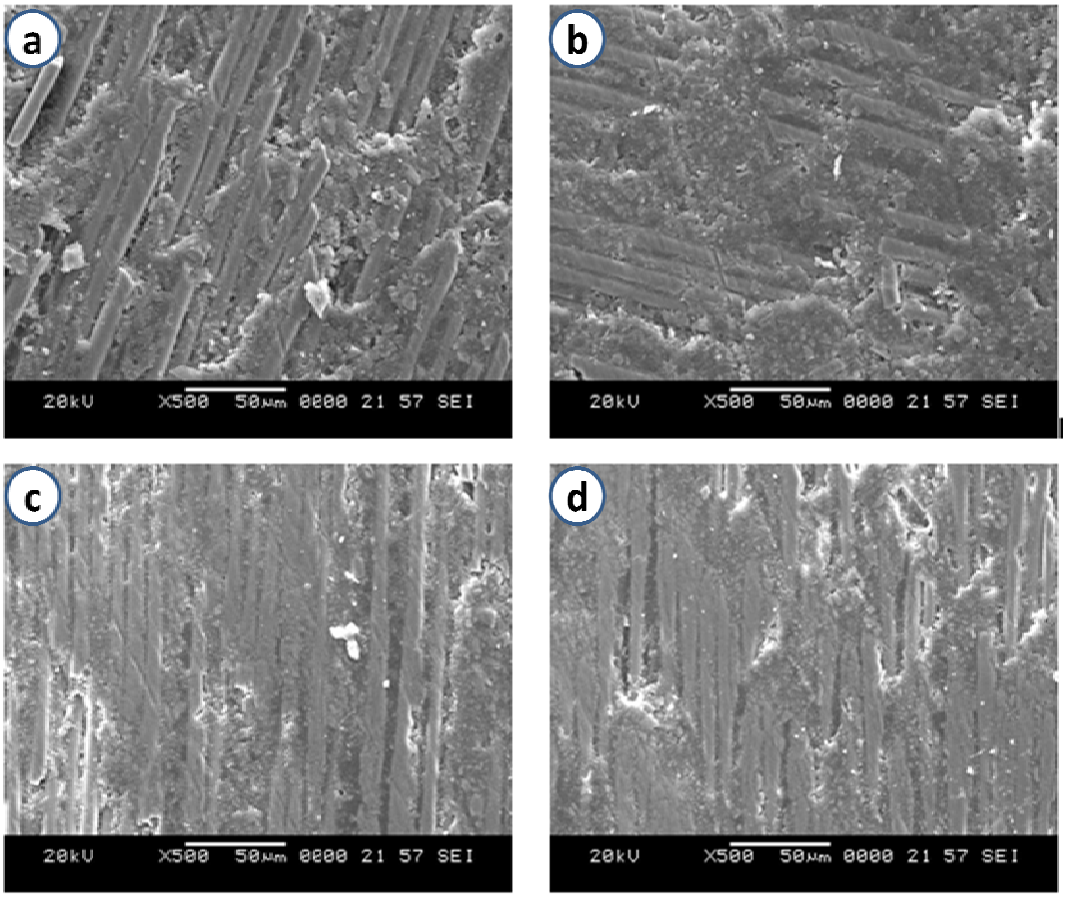

Fig 8.Surface topographies of composite specimen (a).EG0, (b) EG2.5, (c) EG5 and (d) EG7.5 composites. (Sliding conditions: Load 15N, distance 80m and speed 200 rpm)

All PTW filled epoxy/glass composites performed well with 600 SiC paper and EG7.5 composites exhibited least wear loss. This trend clearly indicates an existence of relationship between size of abrasive particles and content of filler in epoxy/glass composite systems. Under 120 SiC paper, adding a small amount of PTW filler (2.5 wt%) to epoxy/glass composites has reduced wear loss by 22%. Further increase of whisker content has increased wear loss and EG7.5 composites exhibited wear loss higher than EG0 composites. EG5 composites has shown 23% reduction in wear loss in case of 320 SiC paper and EG7.5 composites has shown 40% reduction in wear loss in case of 600 SiC paper in comparison to EG0 composites. These results indicate beneficiary effect of adding PTW into epoxy/glass material systems.

C. Worn Surface Morphology

The worn surface topographies of composites run under maximum conditions considered in test and for 600 SiC abrasive paper is presented in Fig 8a-d. SEM pictures indicated different trends in severity of wear. The severity of abrasive wear, i.e. micro-cutting [8] on the worn surfaces of EG0 composites can be observed in Fig 8a. Some instances of wear debris collected on surface and pits formed between glass fibersdue to removal of matrix material can be seen in case of EG0 composites. Altogether a severe damage of surface can be evidenced from micrograph of EG0 composites. This indicates poor abrasive wear property of pristine epoxy/glass composites. On other hand, PTW filled composites showed smoother surfaces with lesser damage. Even though some instances of fiber damage can be observed in case of EG2.5 and EG5 composites (Fig 8b and c), glass fibers are well protected and remain attached to composite surface. Matrix loosening [6] and some wear scar marks on fibers by SiC abrasive particles can be observed in these micrographs. SEM picture of EG7.5 composite shows a pit formed which may due to SiC abrasive. The sheared and compressed fiber impressions can also be observed in case of EG7.5 composites. The SEM findings are in line with abrasive wear data presented in Fig 7.

IV. CONCLUSIONS

A series of epoxy/glass/PTW composites with varying PTW content were prepared and evaluated for abrasive wear performance. From this experimental investigation, following conclusions can be arrived.

1. COF decreased with normal load and has shown mixed trend with sliding distance, abrasive grit size and PTW content.

2. Abrasive wear loss increased with sliding distance and applied load. Performance ranking of epoxy/glass/PTW composites under abrasive wear depends upon grit size. No composite performed best in all abrasive conditions and deciding optimum content of filler to minimize wear loss is a multi-criteria optimization problem.

3. SEM pictures revealed that micro-cutting is dominant mechanism in case of EG0 composites and matrix fracture as prevalent mechanism in case of epoxy/glass/PTW composites.

This study revealed that PTW can be used as a filler to improve abrasive wear resistance of epoxy/glass composites.

ACKNOWLEDGMENT

Authors remain grateful to Director, Principal, and Vice-Principal of St. Joseph Engineering College, Mangalore, fortheir support to carry out this work. Authors also thank Metallurgy and materials engineering department, NITK Surathkal for providing SEM facility.

REFERENCES

[1] M. J. Neale and M. Gee, *Guide to Wear Problems and Testing for Industry*, New York, USA: William Andrew Publishing; pp. 3-8, 2001.

[2] J.J. Rajesh, J. Bijwe and U.S.Tewari, "Influence of fillers on abrasive wear of short glass fibre reinforced polyamide composites", *Journal of Materials Science*, vol. 36, pp. 351-356, 2001.

[3] J. Bijwe, C.M. Logani and U.S. Tewari,"Influence of fillers and fiber reinforcement on abrasive wear resistance of some polymeric composites", *Wear*, 138, pp.77-92,1990.

[4] N. Mohan, S. Natarajan, S.P. KumareshBabu and Siddaramaiah, "Investigation on two body abrasive wear behavior of silicon carbide filled glass fabric–epoxy composites", *Journal of Minerals & Materials Characterization & Engineering*, vol.9, no.3, pp. 231-246, 2010.

[5] B. Suresha, B.N. Ramesh, K.M. Subbaya, B.N.Ravikumar and G. Chandramohan, "Influence of graphite filler on two-body abrasive wear behavior of carbon fabric reinforced epoxy composites", *Materials and Design* 31, pp. 1833-1841, 2010.

[6] N. Mohan, S. Natarajan and S.P. KumareshBabu, "Abrasive wear behavior of hard powders filled glass fabric-epoxy hybrid composites", *Materials and Design*, 32, pp. 1704-1709, 2011.

[7] A.P. Harsha and U.S. Tewari, "The effect of fiber reinforcement and solid lubricants on abrasive

wear behavior of polyetheretherketone composites", *Journal of Reinforced Plastics and Composites*, vol. 23, no. 8, pp. 751-766, 2003.

[8] B.Suresha, G. Chandramohan, Kishore, P. Sampathkumaran and S. Seetharamu, "Mechanical and three-body abrasive wear behavior of SiC filled glass-epoxy composites", *Polymer Composites*, 33, pp. 1020-1025, 2008.

[9] T. Zaremba and D. Witkowska, "Methods of manufacturing of potassium titanatefibres and whiskers. A review," *Materials Science- Poland*, vol. 28, no. 1, pp. 25–41, 2010.

[10] M. Sudheer, RavikanthaPrabhu, K. Raju, and ThirumaleshwaraBhat, "Modeling and Analysis for Wear Performance in Dry Sliding of Epoxy/Glass/PTW Composites Using Full Factorial Techniques," *ISRN Tribology*, vol. 2013, Article ID 624813, 11 pages, 2013. doi:10.5402/2013/624813

[11] N.P. Suh, *Tribophysics*. New Jersey: Printice-Hall; 1986.

[12] R.I. Trezona, D.N. Allsopp and I.M. Hutchings, "Transitions between two-body and three-body abrasive wear: influence of test conditions in the microscale abrasive wear test", Wear, 225-229, pp. 205-214, 1999.

Rolling Element Bearing Condition Classification Using Hoelder Exponents

Kumar H. S.[#1], Dr. Srinivasa Pai P.[#2], Dr. Sriram N. S.[£3], Vijay G. S.[$4]
[#]*Department of Mechanical Engineering, NMAM Institute of Technology, Nitte, Karnataka State, 574110.*
[1]urkumar2006@rediffmail.com' [2]srinivasapai@rediffmail.com
[£]*Department of Mechanical Engineering, Vidya Vikas Institute of Engineering and Technology, Mysore, Karnataka State, 570028.*
[3]nittesriram@yahoo.com
[$]*Department of Mechanical and Manufacturing Engineering, Manipal Institute of Technology, Manipal, Karnataka State, 576104.*
[4]*vgs.mpl@gmail.com*

***Abstract*— Machinery condition monitoring has gained increasing interest in recent years, due to the need to decrease the amount of down time in the industries and to reduce the chances of serious damages and losses caused by failures. Rolling Element Bearings (REBs) are critical components in rotary machines and Condition Monitoring (CM) of REB is essential for enhancing productivity and safe running of the machine. Bearing fault detection, however, still remains a challenging task because most of the fault related signatures are non-stationary. The ability to efficiently detect non-stationary, non-periodic, transient features of the vibration signal makes the wavelet analysis a demanding tool for condition monitoring. Hence, bearing fault detection and diagnosis is an integral part of the preventive maintenance procedures. In this paper, vibration signals for three conditions of a deep groove ball bearing Normal (N), defect on inner race (IR) and defect on outer race (OR) were acquired from a customized bearing test rig, under one load and one speed conditions. Vibration signals collected from the different conditions of the bearing indicate variation in singularity that can be measured by Hoelder exponents. Accordingly, the Hoelder exponents were extracted using wavelet transform for different conditions of the bearing. The variation of the Hoelder exponents for defective bearing conditions with respect to normal bearing have been analysed by employing the statistical process control concept. This method lends itself for effective implementation in practical REB condition monitoring.**

***Keywords* — Rolling Element Bearing, Hoelder exponent (HE), Continuous wavelet transforms (CWT), statistical process control**

I. INTRODUCTION

Condition Monitoring (CM) of REB is needed for enhancing productivity and life of the machines. A reliable bearing health CM and failure diagnostic technique has been the subject of focus in industries to prevent machinery performance degradation and catastrophic failure of machine [1]. From the history of maintenance, traditional maintenance strategies, such as run to break down and preventive maintenance are widely applied. These traditional maintenance strategies are non- economical and they may lead to under-maintenance or over-maintenance. To overcome this problem, condition based maintenance (CBM) is widely used. The successful implementation of CBM depends on accurate identification of health condition of machinery which is realised through condition monitoring systems. Condition monitoring means identification of health condition with information collected from machinery. Generally, the information used can be based on vibration, acoustic emission, temperature, etc. The commonly used technique in fault detection is vibration signature analysis, as it provides comprehensive information about the condition of the machine [2].

The vibration signals produced by defective bearings can be analysed by variety of signal processing techniques and have proved to be effective in CM applications [3]. The widely used techniques are: time domain, frequency domain and time-frequency domain techniques. In the time domain method, the fault is detected by monitoring the variation of some statistical indices like crest factor, root-mean square value and kurtosis. The frequency domain method is based on the transformation of the time domain signal into the amplitude versus frequency space. The advantage of frequency domain analysis over time domain analysis is its capability to easily identify and separate certain spectral components of interest. Frequency based techniques are not suitable for the analysis of non-stationary signals that are generally related to machinery defects. Non-stationary signals are analysed using time-frequency domain techniques such as Short-Time Fourier Transform (STFT),

Wigner-Ville distribution, spectral kurtosis or Wavelet Transform (WT). In bearing fault diagnosis, WT is a widely used technique because it does not contain cross terms as those in Wigner-Ville transform, while it can provide a more flexible multi-resolution solution than the STFT [4].

Literature survey on singularity analysis reveals that for a rotating machine, its vibration signals with different types of malfunctions often have different singularities. Signals with strong singularity are often very disorderly and will reverse itself more frequently, while weak singular signals are often very smoothing [5]. Hence singularity analysis of vibration signals can be effectively used to classify the different conditions of REB.

The Lipschitz exponent or Hoelder exponent (HE) is a good index for singularity measure [6]. Peng et al. [5] used wavelet transform modulus maxima (WTMM) to analyse singularity characteristics of vibration signals acquired from rotating machines, for comparing different faults like imbalance, oil whirl, coupling mis-alignment and rub impact. They concluded that HE obtained by WTMM provide quantitative description of the machine condition. Usually, larger HE indicates a regular point in the signal, while smaller HE indicates a singular point.

Lipschitz exponents have been used for health monitoring. Hambaba and Huff used HE to detect presence of defects in gears [7]. Robertson et al. [8] used HE to detect damage in structures and indicated that HE is very damage sensitive. Qiang Miao et al. [2] used HE to describe the health condition of the machine. They proposed a Kurtosis based health index, which could be used for maintenance decision-making. Loutridis et al. [9] presented a new method of fault detection based on HE. They showed that HE for each type of fault gave a constant value, which was not affected by load or speed, and thus they used HE to classify gear faults. Qiang Miao et al. [10] proposed a novel method for the identification of characteristic components in frequency domain based on singularity analysis. Lipschitz exponent function was constructed from the signal through wavelet-based singularity analysis. Autocorrelation transform was employed to extract the periodic exponents.

The focus of this work is to illustrate the use of HE for REB condition classification. This is accomplished by using statistical process control concept, which provides an effective method in practical REB condition classification. The organization of the paper is as follows- Experimental details, Hoelder exponent, statistical process control approach, bearing condition classification, result and discussions, and conclusion.

II. Experimental Details And Data Collection

A photographic view of the customized test rig used for extracting bearing vibration signals is shown in Figure 1. It consists of a horizontal shaft mounted on a support bearing (right) and a test bearing (left). Radial load on the test bearing can be applied through a hydraulic loading arrangement. Two accelerometers are mounted on the housing of the test bearing. The accelerometers are connected to signal conditioning amplifier and to Data Acquisition system (DAQ) hardware installed in a computer through connecting cables. A customized LAB VIEW (.vi) program is prepared which collects the signals at specified sampling rate and stores it in the computer as a .txt file. For each experiment, a separate .txt file is created which is used for further analysis.

In this work, acceleration signals at a sampling rate of 48000 samples per second were collected for 5.08 seconds. Signals were collected under a radial load of 1.7 kN and shaft speed of 622 rpm. Each trial of experiment resulted in a data vector of size 250000×1. Hence for three bearing conditions, one load and one speed, three data vectors were obtained. Each data vector was divided into 25 non-overlapping bins with each bin having 10000 samples. In this paper, the signals collected from accelerometer-X (vertical) were considered for analysis, as the accelerometer signals acquired in Y direction (horizontal) were found to be not very sensitive to the bearing conditions.

Fig.1 Photograph of the bearing test rig.

III. WAVELET TRANSFORM

The wavelet transform is a tool that cuts up data, functions or operators into different frequency components, and then studies each component with a resolution matched to its scale. The use of wavelet transform is appropriate since it gives the information about the signal both in frequency and time domains. The continuous wavelet transform (CWT) of *f (t)* is defined as

$$CWT(a,b) = \int_{-\infty}^{+\infty} f(t)\,\psi_{a,b}(t)dt.$$

where, $\psi_{a,b}(t) = \frac{1}{\sqrt{a}}\psi\left(\frac{t-b}{a}\right) a,b \in R; a \neq 0$

$\psi_{a,b}(t)$ denotes the mother wavelet. The parameter 'a' represents the scale index, which is a reciprocal of frequency. The parameter 'b' indicates the time shifting (or translation) [17].

IV. HOELDER EXPONENT

Many words, such as discontinuity, disorder, smoothness, etc., are often used to describe the geometrical characteristics of signals, but these terms can only give qualitative descriptions. On the other hand, the Lipschitz exponent (α) can give a quantitative description of the geometrical characteristics of signals, and it can represent the regularity of functions, i.e., continuity and differentiability.

Let *f(t)* be a finite-energy function, that is, $f(t) \in L^2$ (R). We call function *f(t)* be Lipschitz α $(n< \alpha \leq n+1)$, at t_0 , if and only if there exists two constants *K* and $h_0 > 0$, and a polynomial $P_n(h)$ of order *n,* such that for $h \leq h_0$,

$$\left| f(t_0 + h) - P_n(h) \right| \leq K \left| h \right|^{\alpha}$$

(1)

A higher Lipschitz exponent α implies better regularity of the function *f(t)*, that is, a more smooth function *f(t)*. The classical tool for measuring the Lipschitz exponent α of the function *f(t)* is to study the asymptotic decay of its Fourier transform F(ω), but this can only give a global regularity condition because the Fourier transform cannot localise the information along the spatial variable *t*. The Fourier transform is therefore not well adapted to measure the local Lipschitz regularity of functions. On the contrary, the wavelet transform can measure the local Lipschitz regularity of functions since the coefficients of the WT are only determined by the characteristics of the neighbourhood of t_0 and the scale *s*.

Let the wavelet transform of the function *f(t)* be defined over (*a, b*), that is, $x_0 \in (a, b)$.We assume that there exist a scale $s_0 > 0$ and a constant C, such that for $\forall\, t \in (a, b)$ and $s < s_0$, all the modulus maximal of $W_s f(t)$ belong to a cone defined by $|\, t\text{-}t_0 \,| \leq Cs$. Then the function *f(t)* is Lipschitz α at t_0 (α is smaller than the exponent number *n* of the vanishing moment of the function *f(t)*, if and only if there exists a constant A such that for all modulus maximal in the cone

$$\log_2 \left| W_s f(t) \right| \leq \log_2 A + \alpha \log_2 s.$$

(2)

Equation (2) shows that the relation between $\log_2 |\, W_s\, f(t) \,|$ and the scale *s* is determined by the Lipschitz exponent α, and the relation is expressed especially clear through the wavelet modulus maximal. It shows that when $\alpha > 0$ the wavelet modulus maximal increases with the scale s, and when $\alpha < 0$, the wavelet modulus maximal decreases with the scale *s*. Equation (2) also offers a simple method to calculate the Lipschitz exponent α of the singularity point, i.e., the Lipschitz regularity at t_0 is the slope of the straight lines that remain above $\log_2 |\, W_s f(t) \,|$, on a logarithmic scale, as follows:

$$\alpha = \frac{\log_2 \left| W_s f(t) \right|}{\log_2 (s)}$$

(3)

Lipschitz or Hoelder Exponent is a tool that clearly provides information about the regularity of a signal [5].

Equation (2) gives an asymptotic relation between wavelet transform and Lipschitz exponent α, and a lot of methods have been proposed to estimate α. The simplest case [12] uses

$$a = 2^{\frac{1}{m-1}\sum_{s=1}^{m-1} \log 2 \frac{Wf(s+1,x)}{Wf(s,x)}}$$

(4)

where *m* is the length of the maxima line that moves from coarser scale to finer scale. The limitation of this

method is that it uses only the first and last point of the maxima line while discards all other points. Hence, Peng et al. [13] proposed another method, in which the object function is:

$$\sum_{s}[\log 2|Wf(s,x)| - \log 2A - \alpha^{*}\log 2s]^{2} \quad (5)$$

Through minimizing Equation (5) at all scales, we can obtain A and α. Then, the problem of estimation is transformed into optimization and this can be solved by non-linear least-square method. Moreover, Hong et al. [14] used linear regression technique which is an easy way to implement. Although linear regression method is a simplification of Equation (2) that gives a conservative result, it is applicable since we only need a description of change of Lipschitz exponent. With this method, we have:

$$\alpha(x) = \frac{\sum_{s=1}^{m}(\log_2|Wf(s,x)| * \log_2 s) - \frac{\left(\sum_{s=1}^{m}\log_2|Wf(s,x)|\right)\left(\sum_{s=1}^{m}\log_2 s\right)}{m}}{\sum_{s=1}^{m}(\log_2 s)^2 - \frac{\left(\sum_{s=1}^{m}(\log_2 s)\right)^2}{m}} \quad (6)$$

V. Statistical Process Approach

WT is applied to the bearing vibration signals for the three conditions of the bearing (N, IR and OR defect) and the wavelet coefficients are extracted using Continuous Wavelet Transform (CWT). Then Hoelder exponents (α) are obtained using Equation (6). The statistical control process concepts are used to classify the bearing conditions. From the literature survey it is observed that decrease in HE indicates decrease in the regularity of the signal/function.

However it remains to establish how great a decrease of the HE values is required to indicate singularity in a signal with any statistical significance. Statistical control limits have to be determined for the HE, using statistical process control [15]. The control limits determined by using statistical process control are based on a normal (defect free) bearing condition. There are four main limits in governing the controllability of the process:

Lower warning limit (LWL) = μ - 2σ
Lower control limit (LCL) = μ - 3σ
Upper warning limit (UWL) = μ + 2σ
Upper control limit (UCL) = μ + 3σ (7)

where, μ is the mean of the feature under consideration as computed for normal bearing condition (defect free) and σ is the corresponding standard deviation.

Initially, μ and σ of the HE for the normal bearing condition are calculated. Then the HE versus time is plotted for each sample of the normal bearing signal. Statistical control limits are determined as given in Equation (7). Then the three horizontal lines UCL, mean and LCL are plotted for normal bearing condition. For defective bearing, similar plots are drawn and the limits corresponding to normal bearing are marked.

VI. Bearing Condition Classification

Once certain types of damage occur in a bearing, a series of impacts will be generated and the measured vibration signals can be expected to contain singularities. This transient behaviour in the vibration signal can provide vital information for their condition monitoring. However, the singularities are often buried in the noise accompanied by structural response, and hence traditional signal processing methods like frequency and short time Fourier transform have difficulties in detecting them. Hence the use of HE is effective for condition monitoring of REB.

VII. Result And Discussions

Figure 2 shows the variation of raw vibration signals for N, IR and OR REB conditions.

CWT is applied to the normal bearing vibration signals to calculate HE. Accordingly μ value is -21.341 and the σ is 2.496. Then control limits are calculated using Equation (7). For the data samples in this work, LCL and μ are negative and hence are not marked in the plots showing the variation of HE as shown in Figure 3(a).

This process is repeated for other bearing conditions (defect on IR and defect on OR). Figure 3(b) and 3(c) shows the plot of variation of HE with the control limits for defective bearing conditions.

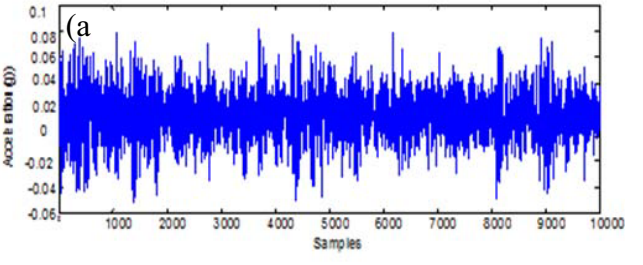

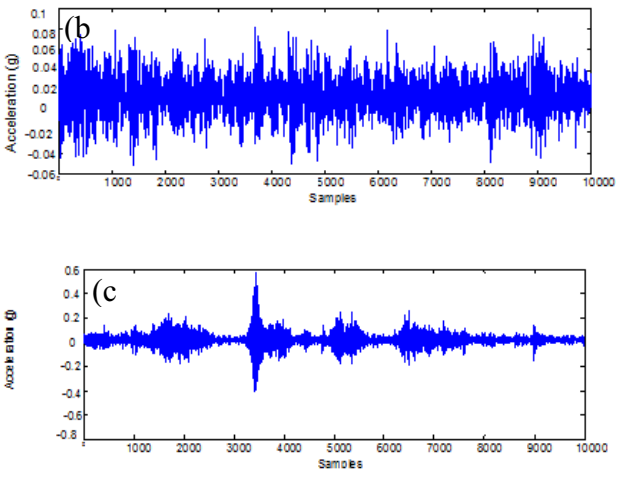

Fig.2 Raw bearing vibration signals for (a) Normal (b)defect on IR and (c) defect on OR.

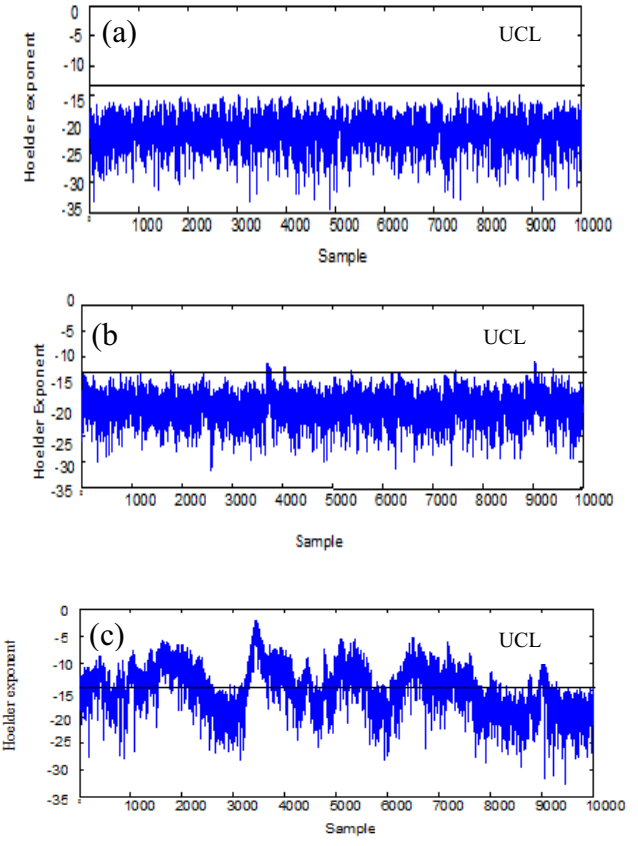

Fig.3 Variation of HE for (a) Normal (b) defect on IR and (c) defect on OR with UCL.

It is clear from the figures that the variation of the HE, particularly above the UCL is more in case of REB with defect on OR, when compared to defect on IR and both show values of HE exceeding the UCL. In this work, UCL is vital as it acts like a threshold for differentiating different conditions of the bearing. For normal bearing condition HE values are lying below the UCL. For bearing with OR defect, more values of HE are above the UCL because the vibration signal has more irregularities or discontinuities which are measured by HE. Thus the use of statistical control limits clearly shows the variation in HE which can be effectively used in classifying the REB condition.

VIII. CONCLUSIONS

This paper explains the application of Hoelder exponents to condition monitoring of REB. The HE can be considered as a parameter which can effectively measure the regularity of the vibration signals. HE is computed using CWT. Control limits are determined using statistical process control. Using statistical process control frame work, the deviations of the HEs above the UCL can be used to distinguish REB with defect on OR and IR from normal bearing. Thus the proposed method provides an effective tool for implementation in practical REB condition monitoring.

REFERENCES

[1] Jie Liu, Wilson Wang and Fai Ma, "Bearing system health condition monitoring using wavelet cross-spectrum analysis technique", Journal of vibration and control 18 (2011), pp. 953-963.

[2] Qiang Miao, Hong-Zhong Huang and Xianfeng Fan, "Singularity Detection in Machinery Health Monitoring Using Lipschitz Exponent Function", Journal of Mechanical Science and Technology 21 (2007), pp. 737-744.

[3] Qiang Miao and Viliam Makis, "An application of the modulus maxima distribution in machinery condition monitoring", Journal of Quality in Maintenance Engineering, Vol. 11 No. 4, 2005, pp. 375-387.

[4] Derek Kanneg and Wilson Wang, "A Wavelet Spectrum Technique for Machinery Fault Diagnosis", Journal of Signal and Information Processing 2 (2011), pp. 322-329.

[5] Z. K. Peng, F. L. Chua and Peter W. Tse, "Singularity analysis of the vibration signals by means of wavelet modulus maximal method", Mechanical Systems and Signal Processing 21 (2007), pp. 780–794.

[6] S. Mallat and W. L. Hwang, "Singularity detection and processing with wavelet", IEEE Transactions on Information Theory 38 (1992), pp. 617–643.

[7] A. Hambaba and A. E. Huff, "Multiresolution error detection on early fatigue cracks in gears", Aerospace Conference Proceedings, 6(2000), pp. 367-372.

[8] A. N. Robertson, C. R. Farrar and H. Sohn, "Singularity detection for structural health monitoring using holder exponents", Mechanical Systems and Signal Processing 17 (2003), pp. 1163–1184.

[9] S. Loutridis and A. Trochidis, "Classification of gear faults using Hoelder exponents", Mechanical Systems and Signal Processing 18 (2004), pp. 1009–1030.

[10] Qiang Miao, Dong Wang and Hong-Zhong Huang, "Identification of characteristic components in frequency domain from signal singularities", Reviw of scientific instruments 81(2010), pp. 035113, 2010.

[11] Vijay G. S., Kumar H. S., Srinivasa Pai P. and N. S. Sriram, "Support Vector Machine based bearing defect classification using wavelet denoised vibration signal", Annual Research Journal, NMAM Institute of Technology, Vol 2, 2012, pp. 27-32.

[12] Struzik Z. R., "Wavelet Methods in (Financial) Time-series Processing," Physica A, Vol. 296, 2001, pp. 307-319.

[13] Peng Z., Y. He, Z. Chen, F. Chu, "Identification of the Shaft Orbit for Rotating Machines using Wavelet Modulus Maxima", Mechanical Systems and Signal Processing, Vol. 16, No. 4,2002, pp. 623-635.

[14] Hong, J. -C., Kim, Y. Y., Lee, H. C., and Lee, Y. W., "Damage Detection Using the Lipschitz Exponent Estimated by the Wavelet Transform: Application to vibration modes of a beam," International Journal of Solids and Structures, 39 , 2002, pp. 1803~1816

[15] Robertson, A.N., Farrar, C. R. and Sohn H., "Singularity detection for structural health monitoring using holder exponents", Mechanical Systems and Signal Processing 17, 2002, pp.1163-1184.

[16] Ka Kian Ton and Keith Worden, "An Application of Holder exponents to Condition Monitoring", sem-proceedings.com.

[17] V. Purushotham, S. Narayanan, Suryanarayana A. N. Prasad, "Multi-fault diagnosis of rolling bearing elements using wavelet analysis and hidden Markov model based fault recognition", NDT & E International 38, 2005, pp.654-664.

GUIDELINES FOR AUTHORS

The contributors are expected to highlight their research work with sufficient details & discussion of results.

The original research paper should be limited to 6 and short communication to 3 printed pages of the journal in double column standard IEEE format. Please refer to IEEE website for the standard format.

Manuscripts must be submitted in both hard and soft copy (in a CD) to the Editor-in-Chief, Annual Research Journal, NMAM Institute of Technology,Nitte-574110, Udupi District, Karnataka.

Enough precaution should be taken to make the manuscript error free.

The papers that are not in the standard format may be rejected

Submission of an article implies that the work described has not been published previously (except in the form of an abstract or as part of a published lecture or academic thesis), that it is not under consideration for publication elsewhere, that its publication is approved by all authors and tacitly or explicitly by the responsible authorities where the work was carried out.

Authors of the selected papers have to send the final camera ready paper (both in MS Word &PDF) for final print

After the review process, the selected papers will be published in the Journal.

Article structure

Subdivision - numbered sections

Divide your article into clearly defined and numbered sections. Subsections should be numbered 1.1 (then 1.1.1, 1.1.2, ...), 1.2, etc. (the abstract is not included in section numbering). Use this numbering also for internal cross-referencing: do not just refer to 'the text'. Any subsection may be given a brief heading. Each heading should appear on its own separate line.

Introduction

State the objectives of the work and provide an adequate background, avoiding a detailed literature survey or a summary of the results.

Material and methods

Provide sufficient detail to allow the work to be reproduced. Methods already published should be indicated by a reference: only relevant modifications should be described.

Theory/calculation

A Theory section should extend, not repeat, the background to the article already dealt with in the Introduction and lay the foundation for further work. In contrast, a calculation section represents a practical development from a theoretical basis.

Results

Results should be clear and concise.

Discussion

This should explore the significance of the results of the work, not repeat them. A combined Results and Discussion section is often appropriate. Avoid extensive citations and discussion of published literature.

Conclusion

The main conclusions of the study may be presented in a short Conclusions section, which may stand alone or form a subsection of a Discussion or Results and Discussion section.

Appendices

If there is more than one appendix, they should be identified as A, B, etc. Formulae and equations in appendices should be given separate numbering: Eq. (A.1), Eq. (A.2), etc.; in a subsequent appendix, Eq. (B.1) and so on. Similarly for tables and figures: Table A.1; Fig. A.1, etc.

NMAM INSTITUTE OF TECHNOLOGY, NITTE – 574110

NMAM Institute of Technology was started in the year 1986, as a part of Nitte Education Trust, Mangalore and is celebrating its Silver Jubilee during 2010 – 11. The Institute is named in fond memory of Nitte Mahalinga Adyanthaya, a distinguished engineer of the district. It is affiliated to the Visvesvaraya Technological University, Belgaum, enjoying academic autonomy and is recognized by the All India Council for Technical Education, New Delhi. It is accredited by the National Board for Accreditation and is certified to the ISO 9001 – 2008 standards for quality education by KEMA, Netherlands. The Institute has been recognized as Lead Institute under TEQIP- I Project of World Bank.

The Institute offers B.E, M.Tech and Ph.D pragrammes in various Engineering and Technology disciplines. The graduate programs comprise of 7 branches of Engineering – Electronics & Communication Engineering, Computer Science & Engineeing, Civil Engineering, Electrical & Electronics Engineering, Information Science & Engineering, Bio-Technology and Mechanical Engineering. The Institute's postgraduate programs include, Master of Technology in five disciplines, Master of Computer Applications and Master of Business Administration. The Visvesvaraya Technological University has opened a postgraduate extension centre at NMAMIT, offering M.Tech in Micro-electronics & Control Systems. Besides these, students also pursue their M.Sc(Eng.) and Doctoral Programs at the Institute. The Institute got academic autonomy in the year 2007, bringing in the much needed flexibility to innovate in terms of curriculum, education delivery and evaluation. Institute entered into collaboration with Penn State University, Harrisburg, USA and started offering 2+2 twinning program in Engineering since 2011.